Geochemistry, Geophysics, Geosystems®

AGU ADVANCING EARTH AND SPACE SCIENCE

RESEARCH ARTICLE
10.1029/2022GC010795

Key Points:

- New technology permits in situ Rb-Sr dating of carefully screened glauconite grains
- Apatite resists Sr exchange, and apatite-bearing glauconite preserves primary Rb-Sr age
- Young and old ages are due to Sr exchange with burial fluids and uptake of radiogenic Sr in secondary carbonate inclusions, respectively

Supporting Information:

Supporting Information may be found in the online version of this article.

Correspondence to:

M. Rafiei,
Mehrnoush.Rafiei@students.mq.edu.au

Citation:

Rafiei, M., Löhr, S. C., Alard, O., Baldermann, A., Farkaš, J., & Brock, G. A. (2023). Microscale petrographic, trace element, and isotopic constraints on glauconite diagenesis in altered sedimentary sequences: Implications for glauconite geochronology. *Geochemistry, Geophysics, Geosystems*, *24*, e2022GC010795. https://doi.org/10.1029/2022GC010795

Received 30 NOV 2022
Accepted 14 MAR 2023

Author Contributions:

Conceptualization: M. Rafiei, S. C. Löhr
Data curation: M. Rafiei, O. Alard
Formal analysis: M. Rafiei, S. C. Löhr, O. Alard
Funding acquisition: M. Rafiei, S. C. Löhr, A. Baldermann, J. Farkaš, G. A. Brock
Investigation: M. Rafiei, S. C. Löhr, O. Alard, A. Baldermann, J. Farkaš
Methodology: M. Rafiei, S. C. Löhr, O. Alard
Project Administration: M. Rafiei
Resources: S. C. Löhr, G. A. Brock
Supervision: S. C. Löhr

Microscale Petrographic, Trace Element, and Isotopic Constraints on Glauconite Diagenesis in Altered Sedimentary Sequences: Implications for Glauconite Geochronology

M. Rafiei[1], S. C. Löhr[1,2], O. Alard[1], A. Baldermann[3], J. Farkaš[2], and G. A. Brock[1]

[1]School of Natural Sciences, Macquarie University, Sydney, NSW, Australia, [2]Department of Earth Sciences, Metal Isotope Group (MIG), University of Adelaide, Adelaide, SA, Australia, [3]Institute of Applied Geoscience, NAWI Graz Geocenter, Graz University of Technology, Graz, Austria

Abstract Glauconite is an authigenic clay mineral that is common in marine sedimentary successions. Dating of glauconite to determine the depositional age of sedimentary sequences has a long history but has fallen into disfavor due to the difficulty of obtaining "pure" glauconite separates. Recent advances in sedimentary petrography and reaction cell mass spectrometry permit rapid in situ Rb-Sr dating of carefully screened glauconite grains. However, glauconite remains susceptible to burial alteration so that successful application of in situ Rb-Sr glauconite geochronology requires improved, microscale constraints on the impact of postdepositional alteration on glauconite Rb-Sr systematics and articulation of robust criteria for identifying grains suitable for geochronology. Here, we address these questions by combining SEM-EDS mineral mapping, geochemical characterization, and in situ Rb-Sr dating of glauconite grains in partially altered lower Cambrian sedimentary sequences from the Arrowie and Amadeus basins in Australia. Our approach provides information at high spatial resolution, representing new insights into the interplay between source material, burial fluids, and diagenetic processes. Among the different glauconite classes, which we classify based on alteration and inclusion type, only the primary apatite-bearing "pristine" glauconite returns an age within the error of the expected stratigraphic age. We attribute the preservation of a depositional Rb-Sr age to the influence of Sr-rich, alteration-resistant apatite and the limited permeability of the clay-rich strata hosting these grains. We conclude that our combined petrographic–geochemical screening approach holds considerable potential for identifying the best preserved glauconite grains for in situ Rb-Sr geochronology.

1. Introduction

The sedimentary record provides us with a unique window into the coevolution of life and the Earth System. Determining the long-term evolution of our dynamic Earth and, in particular, identifying the triggers and responses to transient perturbations requires precise chronological control permitting the correlation of geographically distant localities (Du Vivier et al., 2014; Griffis et al., 2018, 2019). The most widely used radiometric techniques for obtaining absolute depositional ages for sedimentary sequences are presently U-Pb zircon dating of volcanic ash (Du et al., 2020; Schaltegger et al., 2015; Wotzlaw et al., 2014), $^{40}Ar/^{39}Ar$ dating of lava flows (Jourdan et al., 2005, 2009) and Re-Os dating of organic-rich black shales (Kendall et al., 2004, 2006; Lúcio et al., 2020). Improvements to these chronometers allow precise dating and profile correlation and have resulted in major advances in our understanding of the triggers, pace, duration, and geographic extent of major environmental perturbations such as the Cryogenian and Paleozoic (de)glaciations (Cox et al., 2018; Griffis et al., 2018, 2019; Prave et al., 2016; Rooney et al., 2014; Wang et al., 2019; Zhou et al., 2019).

Nevertheless, dating sedimentary sequences remains amongst the most challenging tasks in geochronology as appropriate target lithologies such as volcanic ash beds and black shales are often restricted to specific tectonic or environmental settings, such as volcanically active margins or anoxic marine basins (Huff et al., 1992; Zhao et al., 2019). Further, these geochronologic systems are not immune to postdepositional perturbation or alteration (Straeten, 2004). The scarcity of appropriate lithologies in many marine sequences has therefore hampered attempts at stratigraphic correlation or precise constraints on the timing and pace of major phases of Earth System or biological evolution. This is particularly critical in Precambrian sequences, where the lack of macrofossils and well-preserved carbonate sequences commonly prohibits the application of biostratigraphic or chemostratigraphic correlation approaches.

Validation: M. Rafiei, S. C. Löhr, O. Alard, A. Baldermann, J. Farkaš, G. A. Brock
Visualization: M. Rafiei
Writing – original draft: M. Rafiei
Writing – review & editing: S. C. Löhr, O. Alard, A. Baldermann, J. Farkaš, G. A. Brock

Glauconite geochronology is a potential alternative where ash beds or black shales are absent (Bansal et al., 2019; P. E. Smith et al., 1998). Glauconite is an authigenic, green clay mineral that commonly forms mm-scale pellets and occurs in both siliciclastic and carbonate sequences in a wide range of marine and also continental depositional environments spanning the Precambrian to recent (Banerjee et al., 2016). Glauconite forms at or near the sediment-water interface, and is thought to evolve from K-poor but Fe^{3+}-rich smectite (Charpentier et al., 2011; Gaudin et al., 2005) to mature K- and Fe^{3+}-rich glauconite over a time-frame of 10^3–10^6 years (Baldermann et al., 2013; López-Quirós et al., 2019, 2020). As glauconite pellets mature, they grow and equilibrate isotopically with seawater or seawater-derived fluids, facilitating their physical and chemical separation from the ambient sediment matrix, which in turn permits dating of marine sedimentary successions via glauconite geochronology (Clauer et al., 1992).

Although glauconite bulk separates have long been dated using the Rb-Sr (Clauer, 1981; Kelly et al., 2001; Zaitseva et al., 2008), K-Ca (Cecil & Ducea, 2011; Gopalan, 2008), K-Ar (Amireh et al., 1998; Odin, 1982; Rousset et al., 2004) and ^{40}Ar-^{39}Ar (Bansal et al., 2019; Clauer, 2013; P. E. Smith et al., 1998) techniques, frequent mismatches with independent chronostratigraphic constraints mean that glauconite geochronology is currently not widely employed (Cecil & Ducea, 2011; Clauer, 1981; Hurley, 1966; Hurley et al., 1960; Obradovich, 1988; Selby, 2009). Erroneous ages have been attributed to factors including the presence of detrital Rb- and K-bearing phases in glauconite separates (Boulesteix et al., 2020), as well as postdepositional disruption or resetting of the Rb-Sr isotope system by exposure to increased temperatures and/or fluid-rock interactions (Dickin, 2018; Smalley et al., 1987). Various sample preparation approaches, based on improved mineral separation and more aggressive chemical cleaning, have been developed to address these problems, with varying degrees of success (Derkowski et al., 2009; Foland et al., 1984; Grant et al., 1984; Morton & Long, 1980; Odin, 1982; Tóth et al., 2010).

In situ Rb-Sr dating offers a promising new approach to glauconite geochronology. Unlike traditional thermal ionization mass spectrometric Rb-Sr dating which requires the dissolution of bulk sample powders followed by wet chemical separation of Rb and Sr (e.g., Gopalan, 2008), reaction cell mass spectrometry (ICP-MS/MS) resolves the spectral overlap of ^{87}Rb and ^{87}Sr via the addition of a reaction gas (e.g., N_2O) to a reaction cell (Gorojovsky & Alard, 2020; Hogmalm et al., 2017; Redaa et al., 2021; Tillberg et al., 2017, 2020; Zack & Hogmalm, 2016). Rb is measured on-mass while Sr isotopes are measured as mass-shifted oxides, allowing quantitative on-line separation of ^{87}Rb and ^{87}Sr. When combined with recent advances in sedimentary petrography (e.g., Han et al., 2022; Rafiei & Kennedy, 2019; Rafiei et al., 2020) this approach permits rapid in situ Rb-Sr dating of carefully screened glauconite grains (Farkas et al., 2018), potentially resolving the limitations of traditional glauconite geochronology and opening up a range of new applications (Scheiblhofer et al., 2022). However, despite the promise of this new approach, glauconite remains susceptible to burial alteration (Bansal et al., 2020; Guimaraes et al., 2000). Successful application of in situ Rb-Sr glauconite geochronology therefore requires improved, microscale constraints on the impact of postdepositional alteration on glauconite Rb-Sr systematics, as well as articulation of robust criteria for identifying grains suitable for geochronology applications.

Here we address this research gap by studying glauconite-bearing, partially altered marine sedimentary sequences of the lower Cambrian age of the Arrowie Basin (South Australia) and the Amadeus Basin (Central Australia). We combine detailed petrographic characterization of glauconite grains by SEM-EDS mineral mapping (Rafiei et al., 2020), in situ laser ablation Rb/Sr dating (Gorojovsky & Alard, 2020; Redaa et al., 2021, 2022; Zack & Hogmalm, 2016) and simultaneous trace element geochemical fingerprinting. The aim of this study is to assess the microscale impact of diagenesis on glauconite embedded in partially altered sedimentary sequences and implications for glauconite geochronology. Our microscale petrographic characterization approach promises to (a) reveal new insights into impact and mechanisms of glauconite diagenesis/alteration and (b) theoretically offers the choice to analyze the least altered glauconite grains. This novel approach yields new insights into the mechanisms and impact of postdepositional alteration on glauconite Rb-Sr systematics and Rb-Sr geochronology. We further consider whether targeting of the best-preserved glauconite grains in partially altered sedimentary sequences can produce stratigraphically meaningful dates, and the circumstances under which ages obtained on altered grains may record a postdepositional "diagenetic event."

2. Materials and Methods

2.1. Geological Setting and Sample Selection

Lower Cambrian sediments from the Ajax Limestone (Arrowie Basin, South Australia; Betts et al., 2018) and the Tempe Formation (Amadeus Basin, Northern Territory; P. M. Smith et al., 2015) host fossiliferous and

glauconite-rich intervals, preserving a record of one of the earliest complex animal ecosystems on Earth. Glauconites in these calcareous to mixed calcareous/siliciclastic rocks show a range of alteration states, as identified via variations in grain morphology and composition, with both heavily altered and more pristine grains preserved. Their age and postdepositional history make these intervals suitable analogs for common glauconite-bearing Proterozoic sequences, but with the advantage of precise chronostratigraphic constraints from bio- and chemostratigraphy (Betts et al., 2018), allowing us to assess the geological significance of in situ Rb-Sr ages.

2.1.1. Ajax Limestone

Nine Ajax Limestone samples were collected from the AJX-M section (Gravestock, 1984), Mount Scott Range, Arrowie Basin, South Australia (Figure 1). Two samples were selected for further study following initial petrographic screening (Ajax_332 and Ajax_356, positions marked on Figure 1). The lower Cambrian Ajax Limestone is part of the Hawker Group, which is predominantly comprised of carbonate successions interbedded with minor siliciclastic intervals. A range of depositional environments from shallow marine to carbonate platform, ramp, and slope have been suggested for the lower Cambrian successions of the Arrowie Basin (Jago et al., 2006), with the carbonate strata interpreted to be shallow water successions (James & Gravestock, 1990).

Although the deposition of the Arrowie sedimentary sequences was strongly affected by regional tectonic activity (Petermann Orogeny with a peak at ca. 550 Ma; Delamerian orogeny at ~500 Ma) (Foden et al., 2006; Jago et al., 2006), petroleum systems maturation modeling indicates that the Cambrian Hawker Group succession is of relatively low-grade thermal maturity and immature for oil generation (vitrinite reflectance between 0.25 and 0.55%R_0) (Carr et al., 2012).

Geochronological data from tuff and shale intervals of the lower Cambrian successions in South Australia (for details see Betts et al. (2018)) and their bio/chemostratigraphic correlation with West Gondwana, Southern Britain, and South China indicate that the Ajax Limestone was deposited around ~519 to ~523 Ma. The two samples selected for further study have expected stratigraphic ages of ~520 Ma, assuming a linear sedimentation rate with no major hiatuses.

2.1.2. Tempe Formation

Tempe Formation samples were obtained from the Hermannsburg_41 core (Figure 1). After detailed petrographic examination of six samples, two were selected for further analysis (H41_307 and H41_320, positions marked on Figure 1). The H41 core was drilled in the Gardiner Range in the northern part of the Amadeus Basin (Central Australia). The Tempe Formation, which is part of the Pertaoorrta Group, was deposited in the intracratonic Amadeus Basin and is mainly comprised of clastic mud- and siltstones with interbedded limestones and cross-bedded glauconitic sandstones (Figure 1; P. M. Smith et al., 2015). Sedimentological examination of the Tempe Formation identified deposition in a range of sedimentary environments spanning shallow marine (lagoon, tidal flat and upper shoreface) to deeper marine (lower shoreface and offshore) settings (Bradshaw, 1991). Based on stratigraphic position and lithofacies, the two samples studied here are associated with the offshore deposits of the Tempe Formation.

The Tempe Formation was deposited during the Australian Ordian Stage, corresponding to Cambrian Series two, Stage four (P. M. Smith et al., 2015) spanning ~514–509 Ma (Peng et al., 2020). An integrated geochemical, mineralogical and sequence stratigraphic study of the Tempe Formation and its correlation with sedimentary sequences across the Centralian Superbasin suggested a maximum age of 511 Ma due to the lack of sedimentation prior to this age (Schmid, 2017). Thermal maturity analyses on the organic-rich intervals of the Tempe Formation in the oil and gas fields across the northern parts of the Amadeus Basin revealed mature source rock units between oil and gas window (Jarrett et al., 2016). Several tectonic and orogenic events in this region, for example, the final stages of Peterman Orogeny, Larapinta Event (~480–460 Ma; Buick et al., 2001; Maidment et al., 2006) and Alice Spring Orogeny (~400–300 Ma; Shaw et al., 1984) have affected to variable degree the preservation and postdepositional history of the Tempe Formation.

2.2. Analytical Methods

2.2.1. SEM Imaging and Mineral Mapping

Samples from glauconite-rich intervals selected for petrographic examination were mounted in epoxy resin (30 mm diameter mounts), diamond polished and carbon coated. For imaging, we utilized a FEI Teneo LoVac

10.1029/2022GC010795

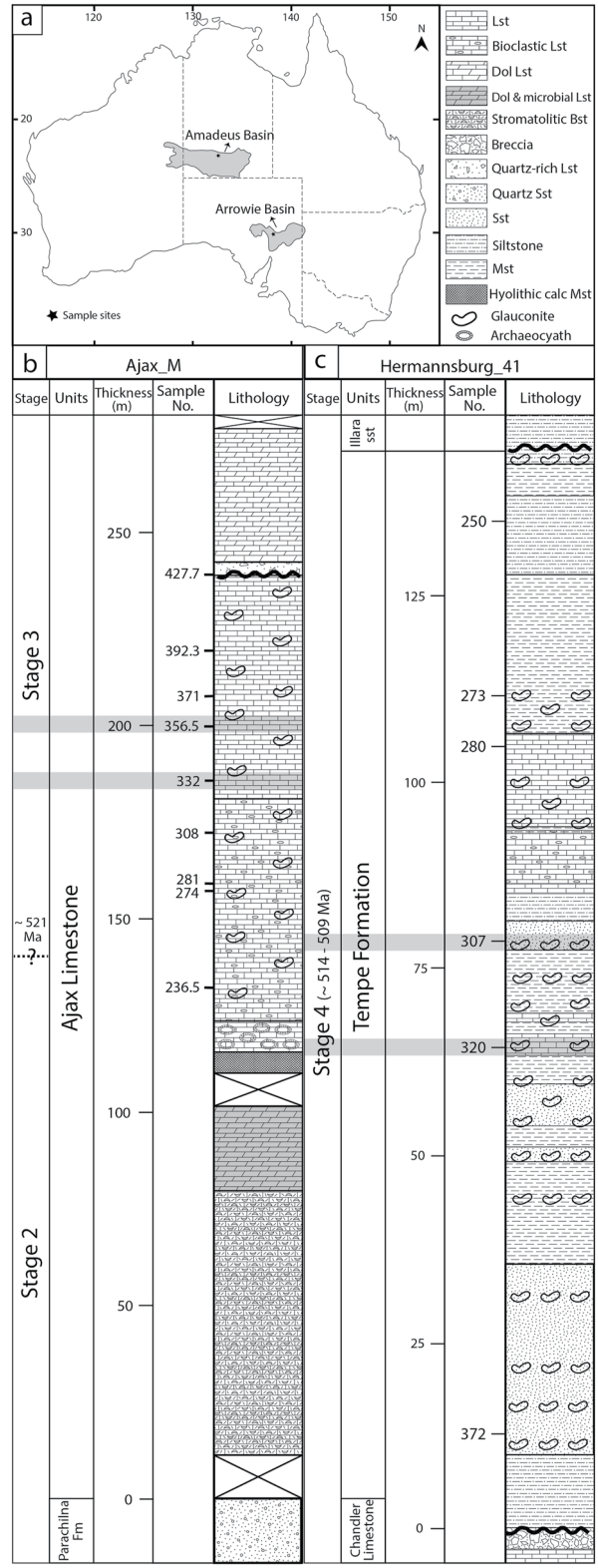

Figure 1. Map showing sampling location and lithostratigraphic column of the studied sections; (a) location of the Arrowie and Amadeus basins and sample sites (modified from Betts et al. (2018) and P. M. Smith et al. (2015)); (b) lithostratigraphic column of the Ajax Limestone at Mount Scott Range in the Arrowie Basin (modified from Betts et al. (2018)); (c) lithostratigraphic log of the Hermannsburg_41 borehole for the interval housing the Tempe Formation (modified from P. M. Smith et al. (2015)). Shaded areas indicate samples used in this study.

field emission scanning electron microscope (SEM) equipped with dual Bruker XFlash Series 6 energy dispersive X-ray spectroscopy (EDS) detectors. The entire mount was scanned to obtain a backscattered electron (BSE) image tileset allowing preliminary sample screening (10 mm working distance, 15 kV accelerating voltage, 100 nm pixel resolution). Subsequently, regions of interest (10–80 in total) of potentially pristine or altered glauconites in each sample were selected for high-resolution BSE imaging (10 nm pixel resolution) and mineral mapping (EDS spectra: 1.5 µm step size, 8 ms acquisition time). Quantitative mineral mapping was carried out using FEI Maps Mineralogy software for automated data collection (both BSE imaging and EDS), whereas the FEI Nanomin software was utilized for the classification of the individual EDS spectra to identify minerals and calculate mineral abundances (for details see Abbott et al., 2019; Frank et al., 2020; Han et al., 2022; Rafiei et al., 2020).

2.2.2. Electron Probe Microanalysis (EPMA)

The chemical composition (Na, Mg, Al, Si, P, K, Ca, Ti, Cr, Mn, Fe, and Ni) of a number of grains for each alteration class was determined using a Cameca SX 100 Electron Microprobe at Macquarie University GeoAnalytical (MQGA) facilities, permitting assessment of glauconite maturity and validation of the petrographic classification of glauconite grain alteration. The operating conditions were 15 kV acceleration voltage with probe current of 20 nA and beam diameter of 1 µm (peak: 30 s and background counting: 15 s). Spots targeted for analysis on representative grains of each class were identified on the basis of BSE images and mineral maps. Glauconite maturity was primarily assessed via the K_2O content (nascent: 1.7%–3.3%; slightly evolved: 3.3%–5%; evolved: 5%–6.6%; highly evolved: >8%; Odin & Matter, 1981).

2.2.3. In Situ Rb/Sr Analysis

After petrographic classification of glauconites (see Section 3.1), we systematically targeted each class as well as cooccurring bioapatites, calcite, and dolomite. In situ Rb/Sr dating of selected glauconites was conducted over the course of five analytical sessions using an Agilent 8900 QQQ ICP-MS/MS coupled to a Teledyne Cetac G2-193 nm laser platform at Macquarie GeoAnalytical laboratories. In addition to Rb and Sr, the concentration of selected trace and major elements (^{26}Mg, ^{27}Al, $^{28}Si^{16}O$, $^{31}P^{16}O$, ^{39}K, ^{43}Ca, ^{47}Ti, ^{51}V, $^{51}V^{16}O$, $^{52}Cr^{16}O$, ^{55}Mn, ^{56}Fe monitored only, ^{59}Co, ^{60}Ni, ^{63}Cu, $^{93}Nb^{16}O$, ^{95}Mo, $^{138}Ba^{16}O$, ^{140}Ce, $^{140}Ce^{16}O$, $^{146}Nd^{16}O$, $^{147}Sm^{16}O$, $^{151}Eu^{16}O$, $^{163}Dy^{16}O$, $^{165}Ho^{16}O$, $^{172}Yb^{16}O$, and $^{175}Lu^{16}O$) was simultaneously measured to search for any inclusions or alterations of glauconite grains. The operating parameters were 85 µm laser spot size, 2.5–5.5 J cm^{-2} fluency, and 5–10 Hz pulse repetition rate. Average depths for each spot analysis are approximately 25 µm in which, it is possible that the ablated volume contains microscale inclusions not identified petrographically on the exposed polished surface. A detailed description of instrument setup, analytical conditions and data reduction is provided in Gorojovsky and Alard (2020) and Table S1 in Supporting Information S1. Reference materials including the glass standard NIST SRM 610, the CRPG Mica-Mg nanopowder (Hogmalm et al., 2017) and the USGS BHVO-2G were utilized as external standards to bracket between every 6–8 sample measurements, calibrate the data and monitor signal drift. To validate data accuracy in each analytical session we also analyzed a phlogopite megacryst (MSN), an igneous phlogopite mineral (MDC; see Redaa et al., 2021) and a GL-O grain mount (Derkowski et al., 2009) of known age (see Supporting Information S1). Data reduction was achieved through an in-house spreadsheet. Consistent with Gorojovsky and Alard's (2020) and Redaa et al. (2022) results, normalization to Mica-Mg and NIST 610 returned the most accurate and reproducible results for $^{87}Rb/^{86}Sr$ and $^{87}Sr/^{86}Sr$ of the standards, respectively, and is the preferred approach used throughout this study. Errorchons were constructed using the IsoplotR package (Vermeesch, 2018), utilizing the ^{87}Rb decay constant reported by Villa et al. (2015), $\lambda_{Rb} = 1.3972 \pm 0.0045 \times 10^{-11}$ a^{-1}, the maximum likelihood model of York et al. (2004), and a 95% confidence limit. Analysis of the GL-O grain mount returned an age of 99.6 ± 9.6 Ma (Figure S1 in Supporting Information S1), which is in agreement with the expected stratigraphic age (99.6 Ma; Selby, 2009).

Trace element concentrations were obtained using the GLITTER software package (Griffin et al., 2008). To this end, average SiO_2 and CaO concentrations obtained by EMPA analysis were used as internal standard for glauconite versus bioapatite, calcite and dolomite, and NIST 610 (Jochum et al., 2011) was used as an external standard. Rb-poor bioapatites and calcite phases that were, petrographically, devoid of impurities were targeted to constrain the initial (seawater) $^{87}Sr/^{87}Sr$. The majority of the spots from these phases revealed values close to expected Cambrian seawater (~0.7091 for ~520 Ma and 0.7090 for ~509 Ma; Denison et al., 1998; Peng et al., 2020).

In order to evaluate deviations in Sr isotopic composition due to postdepositional isotopic exchange or Rb and Sr redistribution, we calculated $\Delta^{87}Sr_t$, expressed in %, based on the measured $(^{87}Sr/^{86}Sr)_m$ and $(^{87}Rb/^{86}Sr)_m$ of each

spot, the expected stratigraphic age (t) of the sample and assuming equilibration with seawater Sr composition ($(^{87}Sr/^{86}Sr)_{0=}$ 0.7090 ± 0.0005, Denison et al., 1998; Peng et al., 2020):

$$\Delta\left(\frac{^{87}Sr}{^{86}Sr}\right)_t = \frac{\left[\left(\frac{^{87}Sr}{^{86}Sr}\right)_m - \left(\left(\frac{^{87}Sr}{^{86}Sr}\right)_0 + \left(\frac{^{87}Rb}{^{86}Sr}\right)_m \times \left(e^{\lambda_{Rb}\times t} - 1\right)\right)\right]}{\left(\left(\frac{^{87}Sr}{^{86}Sr}\right)_0 + \left(\frac{^{87}Rb}{^{86}Sr}\right)_m \times \left(e^{\lambda_{Rb}\times t} - 1\right)\right)}$$

3. Results

3.1. Petrographic Overview

Petrographic and mineralogical characterization shows that Ajax Limestone samples are bioclastic glauconitic limestones comprised primarily of calcite (>80 wt%) with minor glauconite (~5 wt%), bioapatite (~5 wt%) and siliciclastics (mainly quartz and feldspars, ~10 wt%). Trace amounts of illite (mostly as glauconite overgrowths) and iron oxides (microcrystals) are also observed. Quartz and feldspar appear as 10–150 μm sized, mostly angular grains of detrital origin, and more rarely as authigenic fill in moldic microfossil pores. Glauconite grains occur in three forms: (a) as intragranular (microfossils) pore fill (Figure 2a), (b) as replacements of biogenic skeletal remains (Figure 2c) and (c) as oval pellets not associated with biogenic remains (Figures 2b and 2e; 100–200 μm size). Similar authigenic formation of glauconites in the tests of calcareous foraminifera (Baldermann

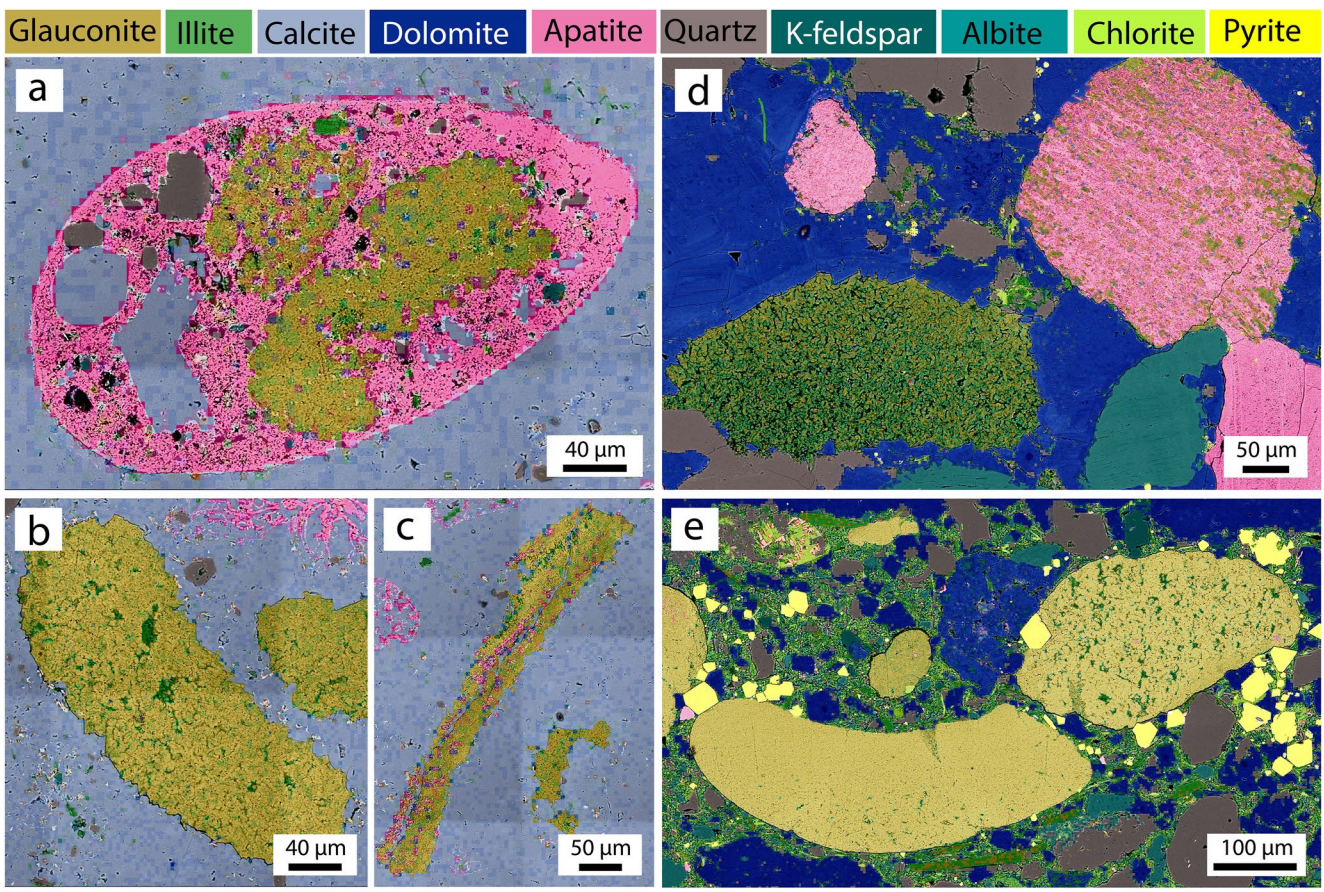

Figure 2. Representative BSE images with mineral overlay demonstrating different occurrence of glauconites in the studied samples; (a) glauconite formation in cavities of a bioapatite fragment embedded in a carbonate matrix showing apatite and calcite microinclusions (sample Ajax_332); (b) glauconite with an oval shape potentially inherited from a pellet substrate and showing patchy illitisation (sample Ajax_332); (c) glauconite replacing a biogenic skeletal fragment with widespread occurrence of apatite inclusions (potentially the remnants of the substrate; sample Ajax_332); (d) heavily and homogeneously illitised glauconite with a porous fabric and a pellet shape (sample H41_320). The intergranular pore spaces in this sample are completely filled with dolomite cement and in some cases with illitised glauconite. The apatite is also intergrown with illite; (e) typical glauconite grains with oval pellet shape in sample H41_307, which contains the most pristine grains. The difference between the glauconite fabric (low vs. high porosity) seemingly resulted in different degrees of illitisation in a single sample. Detrital illite is the main component of the matrix. Other common phases are quartz, dolomite and pyrite.

et al., 2013, 2015) or within the intraparticle pores of bioclasts (Banerjee et al., 2012; Kelly et al., 2001) has been widely reported in the literature.

Samples collected from the Tempe Formation contain glauconite grains of various morphologies occurring in a carbonate or mixed carbonate to clastic matrix. Samples selected for detailed characterization host a combination of oval-to pellet-shaped glauconite grains, some of which are illitised (Figure 2d) and/or contain a range of mineral inclusions such as dolomite, apatite and pyrite. The presence of abraded glauconite grains in glauconitic sandstone (Figure 2e; sample H41_307) is indicative of transportation and intraformational reworking, consistent with cross-bedding of glauconitic sandstone intervals identified by P. M. Smith et al. (2015). Quantitative mineral mapping shows that sample H41_307 is comprised of glauconite (33 wt%, 200–1,500 μm), dolomite (29 wt%), quartz (13 wt%, 30–200 μm), feldspars (10 wt%, 10–200 μm), illite (5 wt%- <10 μm), apatite (5 wt%, micron-sized inclusions to bioclasts of few hundred microns size) chlorite (4 wt%, 10–200 μm), with trace amounts of pyrite and iron oxides. Quartz, feldspar, chlorite, some illite and dolomite grains show abraded and broken margins indicative of a detrital origin, however, some authigenic dolomite and illite grains are present as inter/intragranular pore fill (cement) (Figure 2e). Sample H41_320 is a dolomite-cemented glauconitic sandstone. It shows similar proportions of quartz, glauconite grains and feldspars; however, glauconite grains are homogenously illitised, apatite fossil remains are more abundant (8 wt%), and the intergranular space is entirely occupied by dolomite cement with no fine-grained matrix present (Figure 2d). A further difference to H41_307 is the irregular shape/boundary of glauconite grains in H41_320, which appear to be impacted by the sharp faces of the dolomite crystals comprising the cement, suggesting that glauconite may have formed prior to dolomitization.

3.2. Glauconite Classification

Petrographic (Figures 3 and 4) and major element compositional data (Figure S2 in Supporting Information S1) distinguishes seven classes of glauconite based on the presence of inclusions (primarily apatite and calcite) or the mode and extent of alteration (primarily illitisation). In addition to the above, trace impurities such as iron oxide, pyrite and dolomite were also observed but not considered for petrographic classification purposes as they were not abundant and, apart from dolomite, are not expected to impact on Rb/Sr systematics.

3.2.1. Pristine Glauconite ($GL_{pristine}$)

Pristine grains (or pristine regions within partially altered grains), comprised of unaltered glauconite without detectable mineral inclusions (Figure 3a), were identified in three samples (Ajax_332, Ajax_356, and H41_307) and are here termed $GL_{pristine}$. Pristine grains are mostly oval and well rounded (in the shape of fecal pellets) with smooth surfaces. They display a tightly packed ropy fabric, corresponding to mature glauconite (López-Quirós et al., 2019). Pristine grains are only rarely associated with fossil clasts, but embayment or cracks are filled by illite (Figure 3a). $GL_{pristine}$ in all samples studied here is compositionally mature/highly evolved (~10 wt% K_2O), with elevated Al_2O_3 contents (10–13 wt%) typical of Precambrian and Paleozoic glauconites (Banerjee et al., 2016). $GL_{Pristine}$ in both Ajax samples are similar in composition with average SiO_2 content of 49.46 ± 0.95 and 50.91 ± 0.98 wt%, MgO content of 3.38 ± 0.13 and 3.46 ± 0.07 wt% for samples 332 and 356, respectively. $GL_{Pristine}$ in H41_307 show a more homogeneous but distinctive compositional range compared to Ajax $GL_{pristine}$. They are notably more enriched in SiO_2 (53.41 ± 0.64 wt%), MgO (4.14 ± 0.08 wt%) and Fe_2O_3, but relatively depleted in Al_2O_3 (10.13 ± 0.47 wt%) and K_2O (9.72 ± 0.10 wt%).

3.2.2. Glauconite With Apatite Inclusions ($GL_{apatite}$)

The $GL_{apatite}$ classification refers to otherwise pristine glauconite grains containing apatite inclusions (Figure 3b) and was only identified in sample H41_307. Accordingly, $GL_{apatite}$ has a similar chemical composition to $GL_{Pristine}$ in H41_307. Apatite inclusions are mostly of submicron size and spread sparsely through the grains. Given the commonly observed intergrowth of glauconite and apatite in recent to modern marine sediments (O'brien et al., 1990; Stille & Clauer, 1994; Tóth et al., 2010), and the common occurrence of glauconite in apatite bioclast cavities, we interpret apatite inclusions as cogenetic with glauconite.

3.2.3. Glauconite With Patchy Illite Alteration ($GL_{illitisedP}$)

Glauconite grains hosting illite in pore spaces within their flaky and loosely packed fabric or in the elongate pores/cracks located between bundles of tightly packed bundles of ropy glauconite in otherwise pristine grains (Figure 3d), termed $GL_{illitisedP}$ (illitised patchy), were identified in both Ajax samples as well as in H41_307. Illite, occurring as patchy pore fill exhibits acicular and intergrown habits with pristine glauconite bundles, is

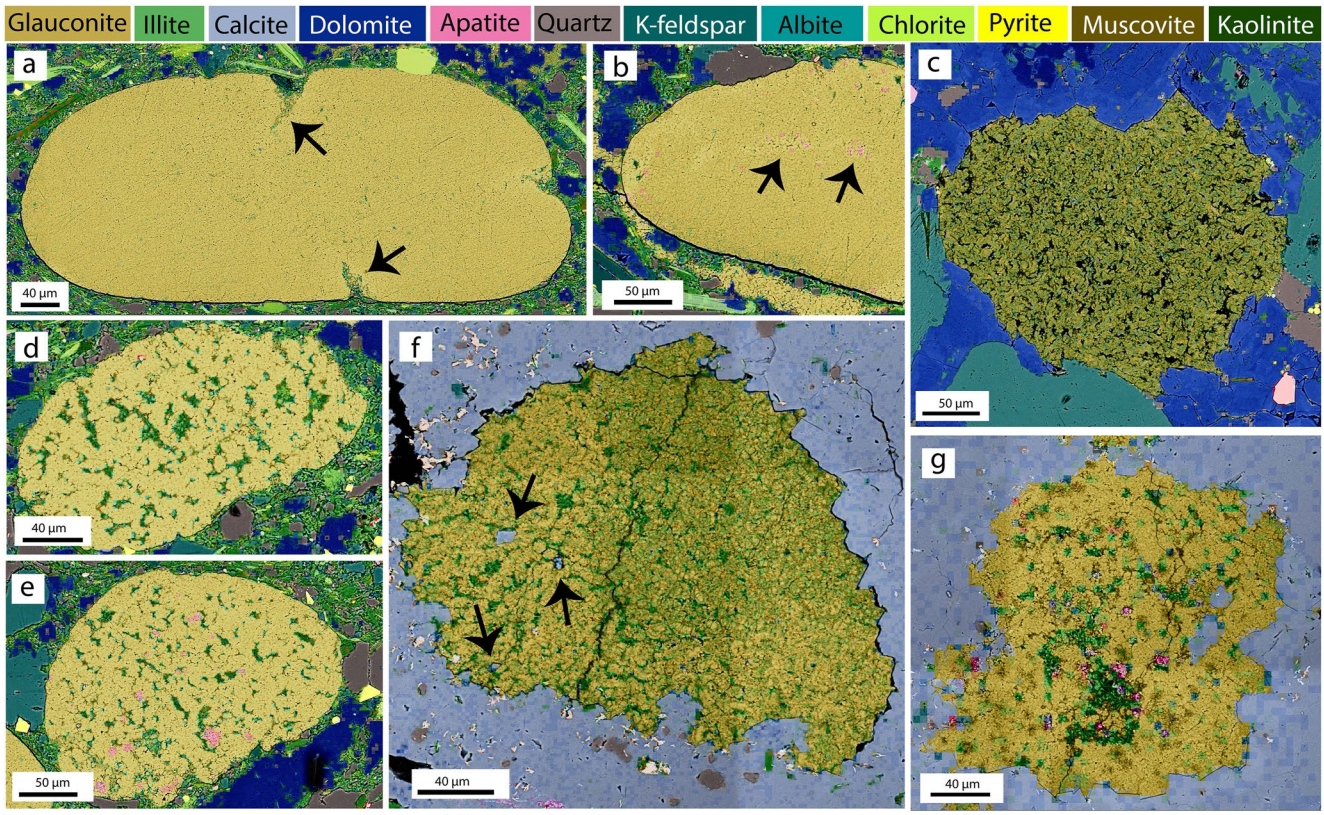

Figure 3. BSE images overlaid by Nanomin mineral maps of the representative glauconite of each defined class; (a) $GL_{pristine}$ glauconite with tightly packed fabric and without impurities in a clay-rich matrix (sample H41_307). Arrows show illitisation occurring through the cracks; (b) Pristine glauconite with apatite inclusions ($GL_{apatite}$) in sample H41_307; (c) A $GL_{illitisedH}$ grain showing homogenous illitisation with a loosely packed fabric and higher porosity (Sample H41_320); (d) A $GL_{illitisedP}$ grain with more porous fabric and patchy illitisation through the elongate pores/cracks located between bundles of ropy, tightly packed glauconite crystals (sample H41_307); (e) A glauconite grain with a pellet shape representative of the GL_{I+A} class in sample H41_307 showing patchy illitisation associated with apatite inclusions; (f) GL_{I+C} grain representing the cooccurrence of patchy illitisation and calcite inclusion (arrows) in sample Ajax_332; (g) GL_{I+A+C} grain showing the presence of patchy illitisation along with apatite and calcite inclusion (sample Ajax_332).

interpreted to have formed via coupled dissolution-precipitation from glauconite or to have precipitated from pore fluids passing through the porous, loosely packed glauconite fabric (Lanson et al., 2002; Pevear, 1999). EMP analysis shows that $GL_{illitisedP}$ has a wider compositional range than $GL_{Pristine}$ and $GL_{apatite}$, reflecting highly localized alteration of the glauconite by diagenetic illite. Illite altered grains are relatively Fe_2O_3 and MgO depleted but K_2O and Al_2O_3 enriched (median concentrations) compared to pristine grains (Figure S2 in Supporting Information S1). We attribute individual analyses showing Fe_2O_3 concentrations greater than observed in pristine samples, together with low concentrations in other major elements (Figure S2 in Supporting Information S1), to the presence of nm-scale iron oxide inclusions, as also evident in BSE images (Figure 4b).

3.2.4. Glauconite With Homogenous Illite Alteration ($GL_{illitisedH}$)

Alteration of glauconite grains resulting in homogenous (as opposed to patchy or localized) replacement of glauconite by illite is here termed $GL_{illitisedH}$, and was identified only in samples Ajax_356 and H41_320. Our petrographic observations suggest that although the initial shape of the pristine glauconite grain is preserved in this class, their original platy, loosely packed and more porous fabric allowed a homogenous alteration to proceed (Figure 3c). Fe_2O_3 and K_2O are depleted whilst Al_2O_3 and MgO are increased and SiO_2 remains unchanged in this class compared to $GL_{pristine}$, $GL_{apatite}$, and $GL_{illitisedP}$.

3.2.5. Illitised Glauconite With Calcite Inclusion (GL_{I+C})

$GL_{illitisedP}$ grains hosting calcite inclusions are here classified as GL_{I+C}. This class was only identified in Ajax samples, which are limestone hosted (Figure 3f). Calcite inclusions are ~5–10 microns in size and are only identified in illitised regions of $GL_{illitisedP}$ grains, suggesting that calcite inclusions formed contemporaneously

10.1029/2022GC010795

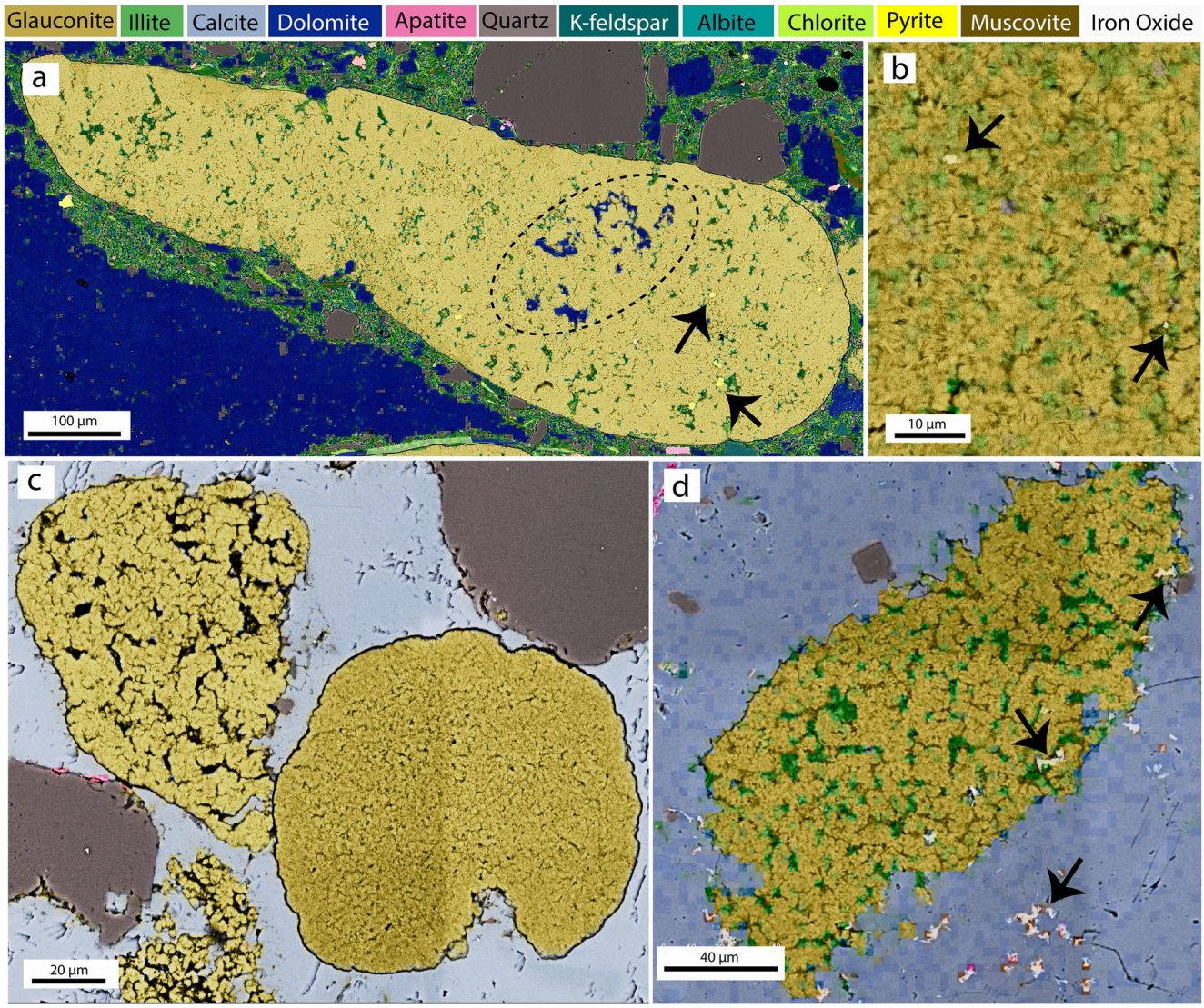

Figure 4. BSE images overlaid with Nanomin mineral maps showing Fe oxide, pyrite and dolomite impurities in example glauconites; (a) An example of patchy illitised glauconite with pyrite (black arrows) and dolomite (black dashed line) precipitation in the pore spaces between the bundles of platy glauconite crystals (sample H41_307). These were rarely observed so are not considered for glauconite classification. (b) nm-scale iron oxides (arrows) between glauconite plates (sample H41_356); (c) Cooccurrence of two different fabric types (tightly packed vs. loosely packed) in well-preserved Ordovician glauconite from Björkåsholmen Fm. (Ceratopyge shale) on Limön Island in the Bothnian Sea. These differences in glauconite fabric suggest that fabric may control the style and extent of alteration by mediating fluid ingress. From sample collection of Wiman (Wiman, 1903); (d) Common occurrence of iron oxides between glauconite plates and throughout the limestone matrix in Ajax samples marked by back arrows (sample Ajax_332).

with illitisation. Where calcite inclusions are present, we find decreased concentrations of major glauconite and illite elements (K_2O, Al_2O_3, Fe_2O_3, etc.) with corresponding increases in CaO. Apart from this, no compositional differences to $GL_{illitisedP}$ are recognized. We distinguish this class from $GL_{illitisedP}$ because calcite inclusions are expected to influence Sr systematics due to the relatively higher content of Sr in carbonates.

3.2.6. Illitised Glauconite With Apatite Inclusion (GL_{I+A})

Where $GL_{illitisedP}$ or $GL_{illitisedH}$ (only in sample H41_320) grains also contain apatite inclusions, we classified them as GL_{I+A} (Figure 3e). This is the only class that is identified in all four samples.

3.2.7. Illitised Glauconite With Calcite and Apatite Inclusions (GL_{I+A+C})

Patchily illitised grains containing both primary (apatite) and secondary (calcite) inclusions are classed as GL_{I+A_C} (Figure 3g), and were only observed in sample Ajax_332.

3.3. $^{87}Sr/^{86}Sr$, Trace, and Major Elements

Up to 12 representative spots per sample for each petrographically defined glauconite class were analyzed by LA-ICP-MS/MS to determine $^{87}Rb/^{86}Sr$, $^{87}Sr/^{86}Sr$ as well as selected major and trace element abundances. The results identify compositional ranges largely consistent with those expected from petrographic and EMPA data, but also identify multiple instances of potential impurities, inclusions or alteration in the laser-sampled volume (subsurface) not evident in mineral mapping data (surface; see Figures 5 and 6). The average trace element concentrations and $^{87}Sr/^{86}Sr$ values of the most pristine grains (after geochemical screening to remove all spots with inclusions) in samples with $GL_{pristine}$ grains ($GL_{illitisedH}$ in sample H41_320), pure bioapatite, pure calcite and pure dolomite are shown in Table 1. These values along with the ideal composition of each mineral (Table S3 in Supporting Information S1) were used to define the endmembers to calculate the mixing lines shown in Figures 5 and 6. Mixing lines are based on linear mixing between these endmembers. The average composition of geochemically screened GL-O grains is also shown for comparison.

3.3.1. Ajax Limestone

In comparison to the average elemental concentration of GL-O grains measured in this study (Table 1), Ajax Limestone $GL_{pristine}$ grains are enriched in trace elements, including Mn, Ni, and Cu, but depleted in Cr. Although $GL_{illitisedP}$ and $GL_{pristine}$ grains in BSE imaging and EDS mineral mapping are petrographically readily distinguished, their compositional ranges largely overlap and are characterized by high Rb, low Sr, low Ca/P and low Ce. The presence of calcite inclusions is characterized by increased Ca and Sr but decreased Rb, relative to $GL_{pristine}$ and $GL_{illitisedP}$, resulting in high Ca/P, low Rb/Sr and moderately increased Ce (REEs). The presence of apatite inclusions, by contrast, increases Sr, P and REEs (incl. Ce) and decreases Rb, resulting in low Ca/P and Rb/Sr but elevated Ce relative to glauconite and illite. On this basis, a substantial proportion of both $GL_{pristine}$ and $GL_{illitisedP}$ contain previously unrecognized calcite inclusions (Figure 5), whereas unidentified apatite inclusions are rare, possibly indicating that calcite inclusions are smaller and more difficult to recognize than apatite inclusions. A few analyzed spots in GL-O grains show the presence of apatite inclusions, with mixing toward the apatite endmember, in agreement with previous findings of Boulesteix et al. (2020). The same criteria confirm the petrographically based classification of GL_{I+C}, GL_{I+A} and GL_{I+A+C} (see two and three endmember mixing arrays between glauconite/illite, calcite and apatite in Ca/P vs. Sr and Ce plots; Figure 5). It is notable that carbonate-inclusion containing spots define a mixing array reaching Ce concentrations that are close to an order of magnitude greater than expected based on mixing between glauconite/illite and pure primary carbonate endmembers. This suggests that carbonate inclusions are compositionally distinct to the calcite comprising the limestone matrix, and potentially of diagenetic origin (Ca/P vs. Ce plot, Figure 5), consistent with the petrographic association between carbonate inclusions and illitised domains noted previously. Finally, several spots with Rb/Sr ~>30 and Sr <80 ppm show significantly more radiogenic $^{87}Sr/^{86}Sr$ than can be accounted for by mixing between glauconite, illite and apatite/calcite endmembers, suggesting diagenetic incorporation of an unidentified component characterized by low Sr content but highly radiogenic Sr composition possibly sourced from the decomposition of detrital feldspar or mica (see discussion).

3.3.2. Tempe Formation

Petrographically and geochemically, H41_307 includes the most pristine grains out of the samples studied, with only a few $GL_{pristine}$ spots unambiguously containing subsurface apatite inclusions (falling along glauconite-apatite mixing line on Ce vs. Ca/P plot; Figure 6). $GL_{pristine}$ and $GL_{illitisedP}$ show a similar compositional range, confirming the difficulty of distinguishing illite alteration geochemically, whereas consistently low Ca contents and the absence of a mixing array toward calcite or dolomite endmembers confirm the absence of carbonate inclusions across all petrographically defined glauconite classes. The trace element composition of H41_307 $GL_{pristine}$ is notably distinct to Ajax $GL_{pristine}$, with elevated Sr (~1 order of magnitude), V, Cr and Cu concentrations but lower Mn, Ni and REEs. This agrees with previous observations made on the basis of major elements contents. Relative to GL-O standard, $GL_{pristine}$ is enriched in V, Mn, Cu and Sr but depleted in Ni and Cr (Table 1). No anomalously radiogenic $^{87}Sr/^{86}Sr$ values were measured in sample H41_307.

The average concentrations of most trace elements in sample H41_320, including Ti, V, Mn, Co, Cu, and Sr in the $GL_{illitisedH}$ spots, are higher than in $GL_{pristine}$ in other samples (Table 1). Both $GL_{illitisedH}$ and GL_{I+A} show a wide compositional range with mixing between three endmembers, that is, glauconite, dolomite and apatite. In addition, two distinct groupings of $GL_{illitisedH}$ are recognized, one with elevated Sr concentrations (seen in

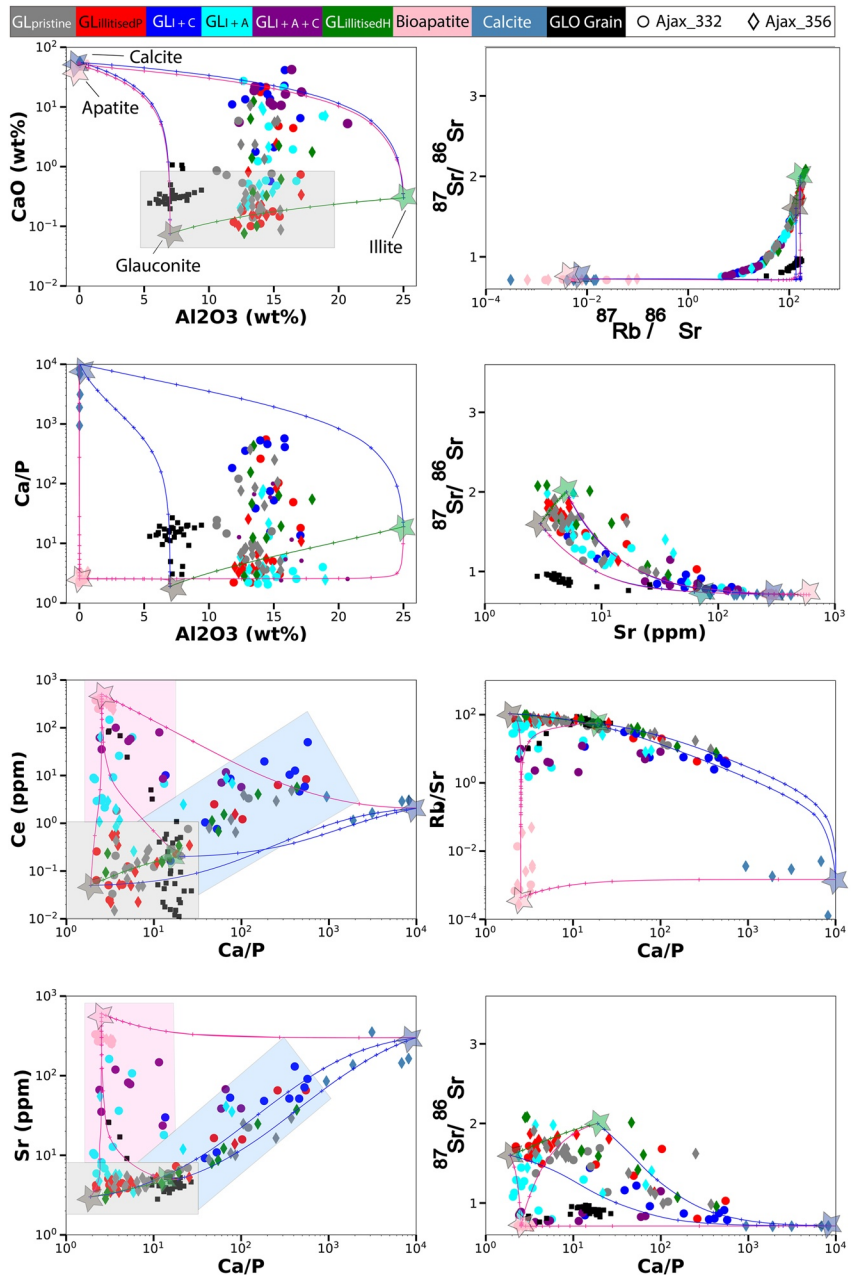

Figure 5. Selected trace and major elements, $^{87}Rb/^{86}Sr$ and $^{87}Sr/^{86}Sr$ of glauconite classes in Ajax Limestone samples analyzed by LA-ICP-MS/MS. The endmembers are calculated based on the average elemental concentrations or isotopic ratios for ideal "pristine" glauconite, illite, dolomite, calcite, and apatite defined in Table S3 of Supporting Information S1. Cut-offs are based on the reclassified $GL_{pristine}$ grains and measured GL-O grains. Gray, blue, and pink shaded areas indicate the approximate compositional ranges for pristine glauconite, calcite inclusion-bearing spots and apatite inclusion-bearing spots, respectively. Axes are a mix of linear and log.

pellet-shaped grains) similar to those in H41_307 $GL_{pristine}$ grains (see Figure 6, Table 1), and one more similar to low-Sr $GL_{pristine}$ of Ajax and GL-O glauconites (seen in various grain shapes and fabrics), resulting in two distinct mixing arrays in Ca/P versus Sr plots. Finally, more than 50% of the $GL_{illitisedH}$ spots and a small proportion of GL_{I+A} define a clear mixing array toward significantly more radiogenic $^{87}Sr/^{86}Sr$ than can be explained by mixing between glauconite, illite and apatite/dolomite endmembers, suggesting diagenetic incorporation of low Sr content but highly radiogenic Sr ($^{87}Sr/^{86}Sr \geq 3$) endmember (Figures 6f and 6g), likely sourced from detrital feldspar or mica. A highly radiogenic influence is evident in both dolomite-inclusion containing and dolomite-free $GL_{illitisedH}$, as indicated by Ca/P versus $^{87}Sr/^{86}Sr$ plots.

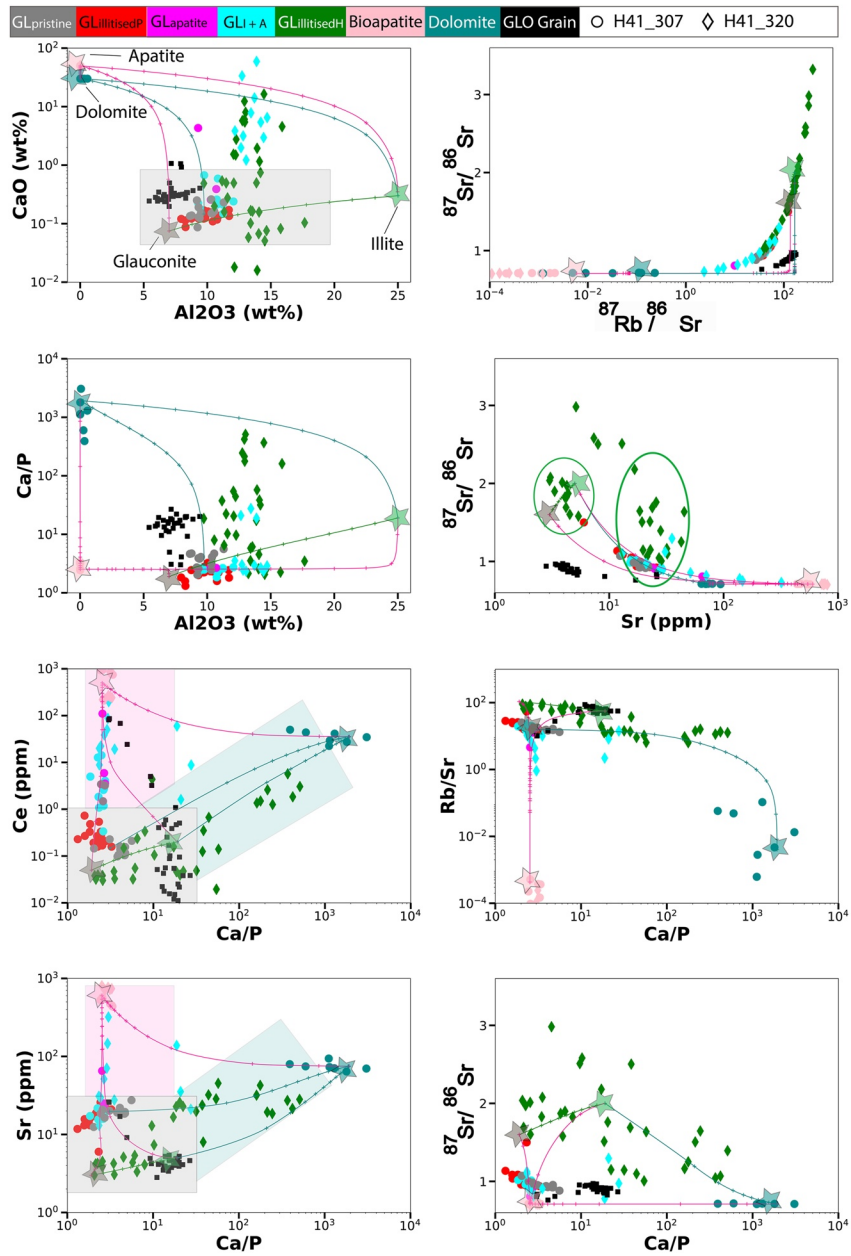

Figure 6. Selected trace and major elements, $^{87}Rb/^{86}Sr$ and $^{87}Sr/^{86}Sr$ values of different glauconite classes in Tempe Fm (H41) samples analyzed by LA-ICP-MS/MS. The endmembers are defined in Table S3 of Supporting Information S1 as presented in Figure 5 with one exception: Here, the carbonate phase is dolomite and the grains with potential dolomite inclusions are highlighted by teal shaded areas. Gray, blue and pink shaded areas indicate the approximate compositional range for pristine glauconite, dolomite inclusion-bearing spots and apatite inclusion-bearing spots, respectively. Green circles in Sr versus $^{87}Sr/^{86}Sr$ graph show the majority of analyzed data points are divided into two groups with low and high Sr content. Axes are a mix of linear and log.

3.4. In Situ Rb-Sr Geochronology

Here, we use the trace element results outlined in the previous section as an additional screen to select the cleanest analyzed volumes/spots for each class to avoid the spots containing unidentified inclusions in constructing Rb/Sr errorchrons. To this end, where anomalous spots closely resemble the composition of another class, we reclassify them as that class, and where they are entirely anomalous, we remove them from the errorchrons. For instance, Ce values of >1 ppm are considered to indicate the presence of apatite or carbonate and Ca/P of >~30 (based on

Geochemistry, Geophysics, Geosystems

10.1029/2022GC010795

Table 1

Trace Element Concentrations (ppm) and $^{87}Sr/^{86}Sr$ Values for Representative Pristine Glauconites in Ajax Samples and H41_307, $GL_{illitisedH}$ in Sample H41_320, Bioapatite, Calcite, Dolomite, and Measured GL-O Grains

Class	Sample	Ti	V	Cr	Mn	Co	Ni	Cu	Rb	Nb	Ce	Sr	Nd	Sm	Eu	Dy	Ho	Yb	$^{87}Rb/^{86}Sr$	$^{87}Sr/^{86}Sr$
$GL_{pristine}$	332-Avg	41	55	22	130	15	1,000	160	290	3.2	0.40	5	0.25	0.06	0.02	0.06	0.02	0.02	125	1.56
	332 ± 1SD	11	3.3	2.9	25	1.0	120	25	17	0.26	0.70	0.49	0.52	0.12	0.03	0.08	0.02	0.01	13	0.115
	356-Avg	51	55	31	110	13	40	94	310	2.2	0.16	4.5	0.08	0.02	0.00	0.02	0.00	0.016	148	1.683
	356 ± 1SD	9.4	2.6	6.0	14	1.3	6.1	83	23	0.33	0.13	0.62	0.08	0.02	0.00	0.01	0.00	0.010	17	0.096
	307-Avg	38	94	55	82	14	13	560	310	3.4	0.14	19	0.06	0.02	0.01	0.05	0.01	0.090	34.8	0.950
	307 ± 1SD	5.4	4.8	6.3	7.7	4.1	2.7	230	25	0.51	0.04	2.6	0.02	0.01	0.00	0.02	0.00	0.030	7.1	0.046
$GL_{IllitisedH}$	320-Avg	156	226	97	1,200	45	27	380	300	2.5	1.1	23	0.60	0.18	0.06	0.39	0.10	0.61	166	1.847
	320 ± 1SD	99	10	10	1,400	14	11	290	25	0.51	1.5	12	0.73	0.21	0.07	0.47	0.13	0.78	73	0.469
Bioapatite	332-Avg	2,000	0.86	0.41	39	1.4	1.1	1.6	0.24	0.01	330	290	220	49	11	30	4.8	3.3	0.00242	0.715
	332 ± 1SD	75	0.14	0.21	18	1.0	0.69	1.3	0.02	0.01	60.	41	35	8.3	1.7	4.5	0.70	0.37	0.00090	0.004
	356-Avg	2,000	1.2	0.58	130	0.71	0.70	1.4	2.9	0.01	320	290	200	43	9.2	29	5.1	3.2	0.021	0.713
	356 ± 1SD	195	0.90	0.41	240	0.35	1.2	0.51	4.8	0.01	47	28	26	5.7	1.2	4.0	1.0	0.88	0.035	0.005
	307-Avg	2,000	0.24	b.d.l.	79	80	12	11	0.14	0.01	870	500	470	120	25	72	13	16	0.00104	0.710
	307 ± 1SD	160	0.14		15	22	3.7	3.6	0.08	0.01	100	53	45	14	1.8	13	2.8	7.4	0.00075	0.002
	320-Avg	1,800	0.28	0.04	200	9.8	0.94	1.1	0.17	0.00	230	770	55	11	3.0	12	2.5	4.6	0.0038	0.707
	320 ± 1SD	91	0.30	0.06	95	7.9	0.26	0.27	0.22	0.00	14	35	3.3	0.77	0.11	0.76	0.23	0.40	0.0042	0.00
Calcite	356-Avg	2,000	0.56	0.10	b.d.l.	b.d.l.	b.d.l.	b.d.l.	0.34	0.03	2.1	250	0.91	0.14	0.02	0.18	0.070	0.12	0.0047	0.709
	356 ± 1SD	15	0.57	0.26					0.41	0.03	1.1	145	0.58	0.10	0.02	0.16	0.060	0.29	0.0053	0.000
Dolomite	307-Avg	1,300	4.9	1.3	b.d.l.	b.d.l.	b.d.l.	b.d.l.	2.5	0.26	35	75	11	2.2	0.53	1.8	0.39	2.7	0.073	0.713
	307 ± 1SD	18	2.9	1.3					2.9	0.33	9.8	9.6	2.4	0.6	0.16	0.91	0.26	1.6	0.086	0.002
GL-O	Avg	31	55	110	35	14	34	16	260	4.8	0.16	4.2	0.07	0.01	0.00	0.01	0.00	0.01	136.8	0.910
	±1SD	7.24	20.43	20.43	6.79	2.66	7.65	6.51	23.34	1.18	0.20	0.65	0.09	0.02	0.01	0.01	0.00	0.01	22.9	0.040

Note. These values are LA-ICPMS measurements obtained after geochemical screening and reclassification of the anomalous data points as described in the text.

the range of Ca/P in GL-O standards) is considered to indicate the presence of carbonate inclusions. The compositional thresholds used for reclassification are shown as shaded areas in Figures 5 and 6.

We then construct a "total" errorchron for all spots analyzed in each sample (Figure 7), including all the altered or unaltered spots, as well as a separate errorchron for each alteration class (calculated ages plotted in Figure 8). Both are anchored by the use of the mean Rb/Sr and $^{87}Sr/^{86}Sr$ measured on pure apatite or carbonate in each sample (Table 1). All the total errorchrons show scattered data with mean square of the weighted deviation (MSWD) of >1, which is expected given the variety of diagenetically altered grains. The number of spots used for errorchrons before and after reclassification as well as the errorchron age, the estimated uncertainty (1σ), 95% confidence interval (CI), initial $^{87}Sr/^{86}Sr$ and MSWD of each errorchron are given in Table 2.

3.4.1. Ajax Limestone

Inclusion of all the analyzed spots on a total errorchron returns an age of 459.1 ± 3.2 Ma, which is ~61 Ma younger than the expected stratigraphic age for Ajax_332 (~520 Ma), whereas the calculated $^{87}Sr/^{86}Sr_{initial}$ of 0.7330 ± 0.0015 is significantly greater than the lower Cambrian seawater ratio of ~0.709 (Veizer et al., 1999). Individual errorchrons for $GL_{pristine}$, $GL_{illiteP}$, GL_{I+A}, and GL_{I+C} classes return similar ages (e.g., ≈450–485 Ma, Table 2). GL_{I+A+C} returns a comparatively older age of 509.3 ± 16.7 Ma (Figure 8) within the error of the estimated stratigraphic age.

The total errorchron for Ajax_356 returns an age of 483.2 ± 1.9 Ma, which is ~37 Ma younger than the estimated stratigraphic age of this sample (~520 Ma), and an $^{87}Sr/^{86}Sr_{initial}$ of 0.7100 ± 0.0005, that is within the error of the lower Cambrian seawater composition (~0.709; Veizer et al., 1999). The errorchrons for $GL_{pristine}$, $GL_{illitisedP}$, and $GL_{illitisedH}$ return ages of 468.9 ± 3.1, 485.9 ± 3.5 Ma and 473.5 ± 6.5 Ma, respectively (Table 2, Figure 8). Apatite-bearing glauconites (GL_{I+A}) return an older age (506.1 ± 6.3 Ma) that is closer but does not overlap the estimated stratigraphic age. Finally, illitised grains containing carbonate inclusions (GL_{I+C}) yield an age of 516.0 ± 6.1, which is thus the closest age to the expected stratigraphic age.

3.4.2. Tempe Formation

A total errorchron for H41_307 returns an age of 484.4 ± 2.2 Ma (Figure 8), which is ~25 Ma younger than the estimated stratigraphic age (~509 Ma), and an initial $^{87}Sr/^{86}Sr$ of ~0.7122 ± 0.0007. Similarly, individual errorchrons for $GL_{pristine}$, $GL_{illistiedP}$ and GL_{I+A} spots return younger ages (495.2 ± 4.4 Ma; 477.5 ± 2.9 Ma; 490.0 ± 4.4 Ma, respectively). $GL_{apatite}$, by contrast, returns an age of 505.1 ± 5.5 Ma with MSWD of 1.4, which is within the error of the expected stratigraphic age.

A total errorchron for H41_320 yields an age of 500.6 ± 4.1 Ma, thus falling well within the error of the estimated stratigraphic age for the Tempe formation (~509 Ma), as well as a radiogenic (nonmarine) $^{87}Sr/^{86}Sr_{initial}$ of 0.7194 ± 0.0015. An individual errorchron for GL_{I+A} returns a much older age (GL_{I+A}: 563.3 ± 13.6 Ma). $GL_{illitisedH}$ returns an age of 487.3 ± 5.1 Ma (Figure 8). The newly added GL_{I+C} class, incorporating all spots with compositional evidence for carbonate inclusions, returns an age of 533.5 ± 10.2 Ma.

4. Discussion

Improved understanding of postdepositional alteration and criteria for identifying grains suitable for geochronology applications are essential prerequisites for the broader application of in situ Rb-Sr glauconite geochronology. We discuss new microscale insights into the mechanisms and impact of postdepositional alteration on glauconite Rb-Sr systematics and Rb-Sr geochronology, enabled by our novel combination of detailed petrographic characterization of glauconite grains with in situ laser ablation Rb/Sr dating and trace element geochemical fingerprinting. We further discuss whether targeting of the best-preserved glauconite grains in partially altered sedimentary sequences can produce stratigraphically meaningful dates, and the circumstances under which ages obtained on altered grains may record a postdepositional "diagenetic event."

4.1. A Fabric/Textural Control on the Cooccurrence of Pristine and Altered Grains?

The common cooccurrence of altered and seemingly well-preserved glauconite grains in a given sample or stratigraphic level prompts the question: why are some glauconite grains altered whilst others remain seemingly unaffected? The main type of glauconite alteration recognized in our sample set is patchy or homogenous illitisation,

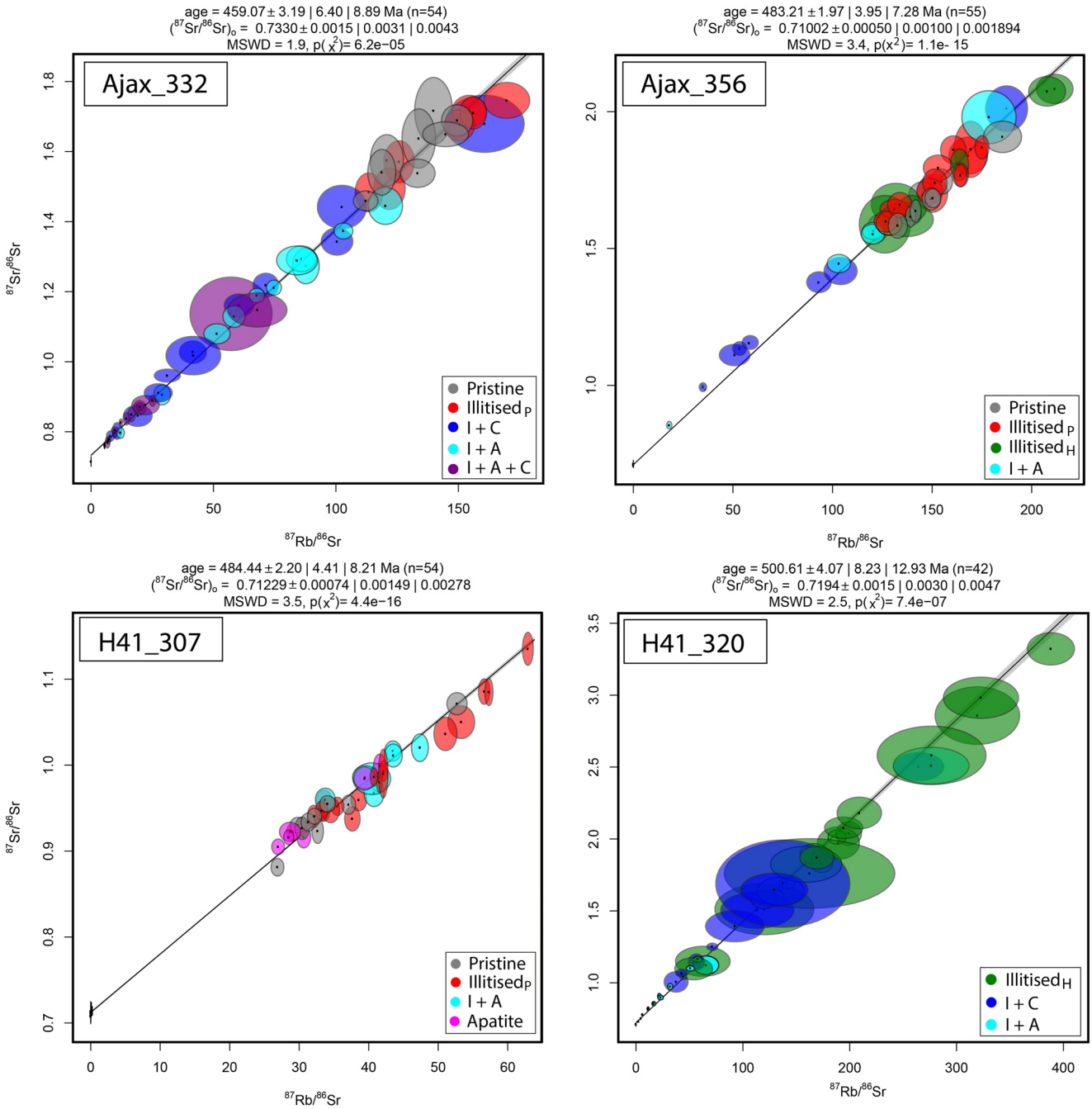

Figure 7. Total $^{87}Rb/^{86}Sr$ and $^{87}Sr/^{86}Sr$ errorchrons constructed using all the analyzed spots including carbonate and apatite data in each sample.

commonly accompanied by the presence of calcite or dolomite inclusions. Systematic differences in the fabric of pristine versus altered glauconite are indicative of a fabric control on the style and extent of alteration. (a) "Pristine" glauconite grains ($GL_{pristine}$) show tightly packed, low porosity fabric and only contain minor patches of illite or calcite inclusions (Figure 3a). We suggest that the tightly packed fabric of pristine glauconite may have limited ingress of burial diagenetic fluids, preserving these grains from extensive alteration. We note, however, that the lower-than expected measured $^{87}Sr/^{86}Sr$ for many $GL_{pristine}$ spots (Table S2 in Supporting Information S1, see also Section 4.3.1) suggest that minor fluid alteration impacted a substantial proportion of even the petrographically "pristine" grains. (b) Patchy illitisation ($GL_{illitisedP}$) is associated with glauconite grains exhibiting distinctly bimodal porosity and ropy fabric, with illite and calcite occurring mainly within elongate pore spaces present

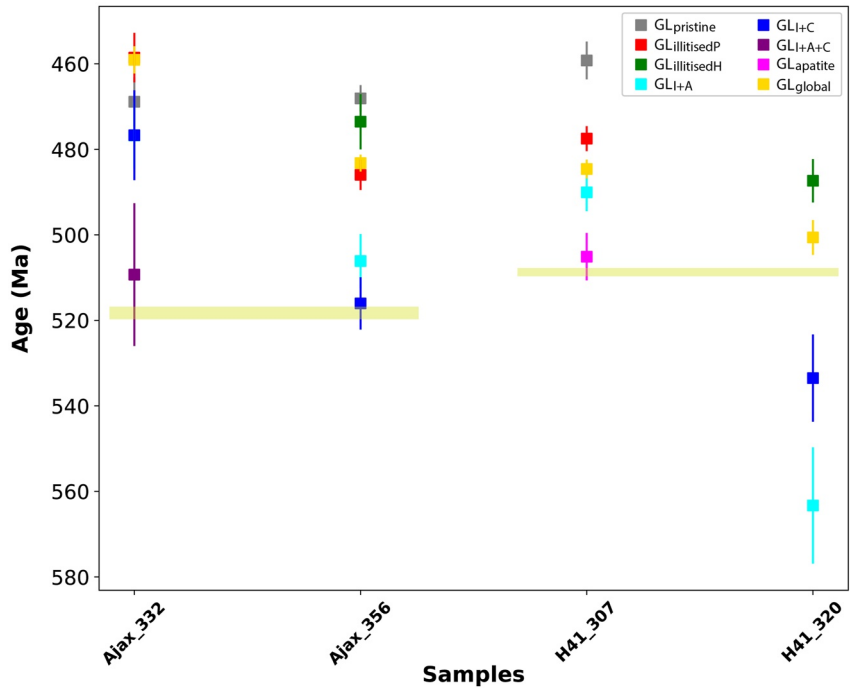

Figure 8. Rb-Sr isotope ages obtained for each glauconite alteration class after geochemical screening and reclassification of the analyzed spots. The expected stratigraphic ages are highlighted by yellow shaded areas for each sample.

between bundles of more tightly packed, "non-porous" glauconite. (c) Homogenous illitisation ($GL_{illitisedH}$), by contrast, is associated with grains showing a more uniformly porous and loosely packed fabric, which is likely to have facilitated even fluid ingress and homogenous rather than patchy illitisation. Furthermore, observation of fabrics associated with each alteration style in samples containing only unaltered mature glauconite (e.g., Figure 4a) demonstrates that the style and extent of alteration are more likely controlled by fabrics, rather than being the product of differing degrees of alteration. We therefore conclude that the cooccurrence of altered and unaltered glauconite is primarily a function of the range of prealteration grain fabrics contained within a particular sample, as well as the magnitude of alteration experienced by a sample.

4.2. Controls on Illitisation of Glauconite and the Significance of Other Inclusions

Postdepositional alteration of glauconites into illite or chlorite is thought to be controlled by the intensity of leaching, as well as pH and redox state of the diagenetic fluids (e.g., Bansal et al., 2020; Guimaraes et al., 2000), in addition to the influence of grain fabric outlined previously. The presence of Fe-(oxy)hydroxides versus pyrite in association with altered glauconite can be used to estimate the local paleo-redox state of the altering fluids (Baldermann et al., 2017). Ajax samples showed ample evidence of Fe-oxides but no pyrite (Figure 4d), which we attribute to alteration under relatively oxic conditions due to a presumably shallower burial setting, which did not generate reduced, organic-acid rich fluids, consistent with the modeled low-grade thermal maturity of the source rocks in Hawker Group succession (Carr et al., 2012). Samples from the Tempe Formation, by contrast, contain pyrite but no iron oxides, indicating alteration under reducing or anoxic conditions. In sample H41_320, this is associated with intensely illitised glauconites carrying elevated amounts of trace elements, as well as highly radiogenic Sr in some spots (Figure 7), likely sourced from the dissolution of Rb-rich detrital phases such as mica and K-feldspar. We attribute these properties to (a) the presence of acidic, reducing fluids formed by thermal maturation of organic-rich source rocks in the region (Jarrett et al., 2016) and (b) the relatively high permeability of the fossiliferous dolostone. In contrast, the intensity of illitisation in sample H41_307 is moderate with only patchy illitisation observed, likely due to the lower permeability of the clay-rich host lithology and the densely packed glauconite texture. Although an abundance of pyrite within partially altered glauconite (Figure 2e vs. Figure 2d) documents the presence of a reducing fluid, the absence of excessively radiogenic Sr (Figure 7) and lower trace element concentrations in sample H41_307 (Table 1) is consistent with less fluid passage and minimal detrital silicate dissolution.

Table 2

Table Showing the Number of Analyzed Spots for Each Class in Each Sample Before and After Geochemical Screening and Reclassification, As Well As the Errorchron Age, the Estimated Uncertainty (1σ), 95% Confidence Interval (CI), Initial $^{87}Sr/^{86}Sr$ and the Mean Square of the Weighted Deviation of the Errorchron Plotted for Reclassified Spots

			Total	$GL_{pristine}$	$GL_{apatite}$	$GL_{illitisedP}$	$GL_{illitisedH}$	GL_{I+C}	GL_{I+A}	GL_{I+A+C}
Ajax_332 (expected age ~520 Ma)	No of spots	Before	51	10	–	11	–	11	9	10
		After	51	9	–	7	–	15	9	11
	Age (Ma)		459.1	468.9	–	458.5	–	476.7	476.8	509.3
	±1σ		3.2	5.7	–	5.8	–	10.5	7.7	16.7
	95% CI		6.4	12.9	–	14.1	–	22.5	17.5	37.3
	$(^{87}Sr/^{86}Sr)_0$		0.733	0.714	–	0.715	–	0.713	0.717	0.724
	±1σ		0.001	0.006	–	0.006	–	0.003	0.005	0.003
	MSWD		1.9	2	–	1.4	–	2	1.5	2.3
Ajax_356 (expected age ~520 Ma)	No of spots	Before	51	17	–	14	10	0	10	–
		After	46	12	–	12	6	9	7	–
	Age (Ma)		483.2	468.1	–	485.9	473.5	516.0	506.1	–
	±1σ		1.9	3.1	–	3.5	6.5	6.1	6.3	–
	95% CI		3.9	6.4	–	7.3	13.8	12.8	13.4	–
	$(^{87}Sr/^{86}Sr)_0$		0.710	0.709	–	0.709	0.709	0.709	0.709	–
	±1σ		0.000	0.000	–	0.000	0.000	0.000	0.000	–
	MSWD		3.4	1.4	–	2	1.5	3.2	1.6	–
H41_307 (expected age ~509 Ma)	No of spots	Before	45	13	3	19	–	–	10	–
		After	44	10	6	18	–	–	10	–
	Age (Ma)		484.4	495.2	505.1	477.5	–	–	490.0	–
	±1σ		2.2	4.4	5.5	2.9	–	–	4.4	–
	95% CI		4.4	9.7	12.8	6.1	–	–	9.6	–
	$(^{87}Sr/^{86}Sr)_0$		0.712	0.710	0.710	0.711	–		0.710	–
	±1σ		0.000	0.001	0.001	0.001	–	–	0.001	–
	MSWD		3.5	3.5	1.4	4.1	–	–	2.5	–
H41_320 (expected age ~509 Ma)	No of spots	Before	43	–	–	–	33	0	10	–
		After	41	–	–	–	19	13	9	–
	Age (Ma)		500.6	–	–	–	487.3	533.5	563.3	–
	±1σ		4.1	–	–	–	5.1	10.2	13.6	–
	95% CI		8.2	–	–	–	10.7	22.3	31.3	–
	$(^{87}Sr/^{86}Sr)_0$		0.719	–	–		0.710	0.713	0.714	–
	±1σ		0.001	–	–	–	0.005	0.005	0.001	–
	MSWD		2.5	–	–	–	0.58	1	4	–

Note. Where anomalous spots closely resemble the composition of another class, they are reclassified.

As noted previously, criteria for identifying well-preserved grains are essential before in situ Rb-Sr glauconite geochronology can be applied more broadly. Different styles or extents of illitisation of glauconite are readily discriminated petrographically. However, most of the $GL_{illitisedP}$ spots show overlapping chemical compositions (both in major and trace elements) with $GL_{pristine}$ grains, consistent with the similar mineral chemistry of illite and glauconite, which is largely distinguished by the low Fe content in illite compared to the higher Fe content in glauconite. Given that our results suggest that Fe liberated during illitisation of glauconite is commonly retained at the microscale, as distinct Fe-bearing microinclusions, this limits the utility of geochemical screening (for potentially petrographically unidentified subsurface alteration) and further suggests that both $GL_{pristine}$ and $GL_{illitisedP}$ grains contain complex intergrowths of altered and unaltered regions. On the other hand, geochemical

screening is able to identify the presence of cryptic or subsurface carbonate and apatite inclusions in petrographically pristine and illitised grains. Ca is barely incorporated into the glauconite structure (Stille & Clauer, 1994); therefore, high levels of Ca and Sr can be attributed to the presence of cryptic Ca-rich carbonate/calcite inclusions. The clear petrographic association between calcite inclusions and illitised domains identifies a late diagenetic origin ~ penecontemporaneous with illitisation for a majority of the carbonate inclusions, as also supported by the mixing array toward anomalously radiogenic Sr measured in calcite-inclusion-bearing grains (Figure S3 in Supporting Information S1). The Ca concentration can therefore be used to screen for the presence of cryptic illitisation and carbonation in $GL_{pristine}$ grains, which is helpful given the otherwise similar chemical composition of $GL_{pristine}$ versus $GL_{illitised}$, although this relationship may not apply in other settings. Apatite inclusions, by contrast, are here interpreted as cogenetic phases with glauconite. Not only are intergrowths of glauconite and apatite in recent to modern marine sediments well documented (e.g., O'Brien et al., 1990; Stille & Clauer, 1994; Tóth et al., 2010), the growth of glauconite in phosphatic bioclast cavities (Figure 2) and the presence of apatite inclusions in both $GL_{illitisedP}$ and $GL_{pristine}$ grains argue for an earliest diagenetic origin, precipitating from seawater and/or seawater-derived pore fluids, or possibly representing the remnants of bioapatite substrates. This is further supported by $^{87}Sr/^{86}Sr_{initial}$ that is close to seawater composition for apatite-bearing grains (Table 2) and the absence of anomalously radiogenic Sr in apatite-inclusion-bearing grains (see Section 4.3).

4.3. Assessing the Geological Significance of Glauconite Rb-Sr Ages

Evolved glauconites that equilibrated isotopically with seawater and were subsequently preserved in a closed system, without being significantly impacted by late stage or burial diagenesis, are ideal candidates for sediment dating applications. This condition, however, may be rare in sedimentary rocks of Proterozoic and even Paleozoic to Mesozoic age, where the Rb-Sr isotopic system is commonly disrupted and partially reset, yielding erroneous glauconite Rb-Sr ages. The Rb-Sr system of mica-type minerals, especially those with interlayer-associated cations such as K^+ (and by inference Rb^+) in glauconite, has been suggested to be susceptible to ion exchange reactions with circulating fluids during diagenesis (Keppens & Pasteels, 1982). Compositional changes accompanying structural modifications during diagenesis and the presence of residual detrital clay materials containing highly radiogenic Sr have been proposed as possible explanations for the less radiogenic Sr (younger ages) and presence of excessively radiogenic Sr (older ages), respectively (Hurley et al., 1960, 1961; Keppens & Pasteels, 1982). Additionally, the dissolution of detrital clays in the host sediment matrix could result in the introduction of more radiogenic Sr into the pore water (Clauer et al., 1982), which can subsequently be incorporated by diagenetic phases precipitating from that radiogenic and nonmarine fluid. Diagenetic processes impacting on the Rb-Sr system fall into these possible scenarios: (a) (partial) equilibration of glauconites and diagenetic alteration products with burial fluids, resulting in a nonmarine (usually radiogenic) $^{87}Sr/^{86}Sr_{initial}$ and, depending on the $^{87}Sr/^{86}Sr$ signature of the fluid, ages that are too young ($^{87}Sr/^{86}Sr_{glauconite} > {}^{87}Sr/^{86}Sr_{fluid}$), unchanged ($^{87}Sr/^{86}Sr_{glauconite} \sim {}^{87}Sr/^{86}Sr_{fluid}$) or too old ($^{87}Sr/^{86}Sr_{glauconite} < {}^{87}Sr/^{86}Sr_{fluid}$); (b) diagenetic loss of Sr and/or incorporation of Rb, resulting in postdepositional increase of Rb/Sr and therefore ages that are too young; (c) diagenetic incorporation of Sr and/or loss of Rb, resulting in postdepositional lowering of Rb/Sr and therefore ages that are too old.

4.3.1. Origin and Significance of Excessively Young Glauconite Rb-Sr Ages

Inclusion-free but partly illitised glauconite ($GL_{pristine}$, $GL_{illitisedP}$, and $GL_{illitisedH}$) within a given sample show similar concentrations of Rb and Sr (Figures S4 and S5 in Supporting Information S1), arguing against significant Rb gain or Sr loss. Thus, the young ages are unlikely to be due to postdepositional perturbation of the Rb/Sr. Alternatively, young ages can be attributed to isotopic exchange with burial fluids. Sr is present at low concentrations in glauconite (typically <10 ppm; Table 1) and is thought to act as an exchange ion where glauconite retains expandable smectite layers (Hower, 1961). Therefore, Sr in glauconite (with potential expandable layers) is likely easily isotopically equilibrated with burial fluids, which typically have high Sr concentrations and are most commonly less radiogenic than the glauconite-hosted Sr (Chaudhuri & Clauer, 1993) due to the ingrowth of radiogenic ^{87}Sr over time in high Rb/Sr glauconites.

The impact of isotopic exchange during diagenesis can be evaluated by considering $^{87}Sr/^{86}Sr_{initial}$ values calculated for both total errorchrons and alteration-class specific errorchrons and by assessing $\Delta^{87}Sr$ values, the latter being a measure of deviation between the measured $^{87}Sr/^{86}Sr$ and the theoretical closed system/unaltered $^{87}Sr/^{86}Sr$. While the uncertainties in our measurements are to the same precision, our results (Figure 7 and Table 2) show that $^{87}Sr/^{86}Sr_{initial}$ from both total errorchrons and alteration-class specific errorchrons are more radiogenic than

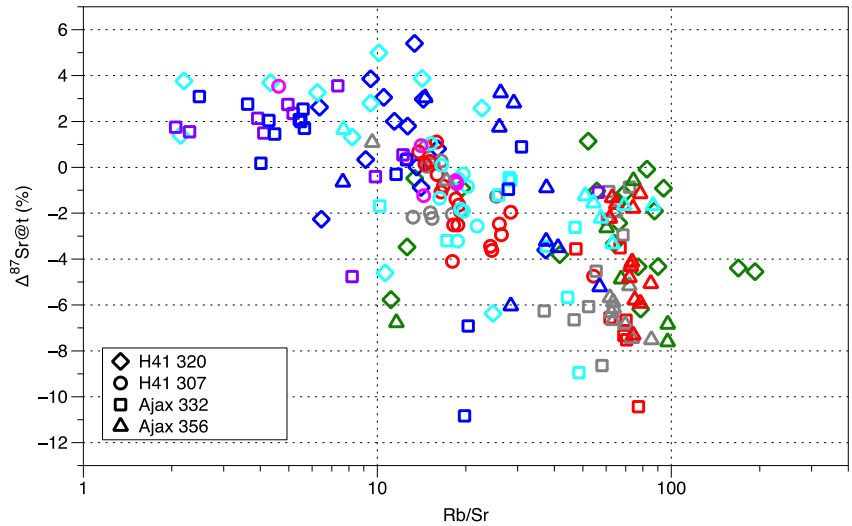

Figure 9. Range of $\Delta^{87}Sr_t$ as a function of Rb/Sr. $\Delta^{87}Sr_t$ is the difference between the analyzed $^{87}Sr/^{86}Sr$ values and the predicted values calculated based on the measured Rb/Sr, estimated stratigraphic age and Sr composition of seawater at that time. Colors indicate glauconite alteration class, as determined by petrographic and geochemical screening; Gray = $GL_{pristine}$; Pink = $GL_{apatite}$; Red = $GL_{illitisedP}$; Green = $GL_{illitisedH}$; Light blue = GL_{I+A}; Dark blue = GL_{I+C}; Purple = GL_{I+A+C}.

the early Cambrian marine $^{87}Sr/^{86}Sr$ (~0.709), consistent with postdepositional Sr exchange. Furthermore, $\Delta^{87}Sr$ values for $GL_{illitisedP}$, $GL_{illitisedH}$ and $GL_{pristine}$ classes are almost uniformly ≤0% (Figure 9), notwithstanding considerable measurement uncertainty (Figure 10), identifying excessively unradiogenic Sr as a common characteristic of classes returning younger Rb-Sr ages. The observation of $\Delta^{87}Sr$ that is commonly <0% in $GL_{pristine}$ spots (mainly Ajax Limestone samples; Figure 9), and with similar $\Delta^{87}Sr$ range as $GL_{illitised}$ spots, further implies (a) the occurrence of finely intergrown pristine glauconite and illite at the sub-μm scale and in the subsurface of analytical volumes, which was not recognized petrographically and could not be screened for geochemically (overlapping compositions; see Section 4.2), and (b) that exchange or partial equilibration with diagenetic fluids did not necessarily result in detectable mineral alteration. We therefore recommend that glauconites with porous and loosely packed fabrics should be avoided even in the absence of evidence for alteration; glauconites with tightly packed fabrics are predicted to be the best targets for in situ Rb-Sr dating.

Whether targeting of altered grains permits dating of postdepositional events is of significant interest as this would broaden the utility of glauconite geochronology. The younger ages obtained for illitised glauconites (between ~475 and ~485 Ma) in H41 samples coincide with time intervals suggested for increased subsidence rates in the Amadeus Basin (around 470 Ma; Shaw et al., 1991) and a tectonothermal event centered on the Arunta Inlier, located northeast of the Amadeus Basin (467 ± 8 Ma; Hand et al., 1999). However, in the broader geological context, the "young ages" measured in several samples are more likely to reflect isotopic mixing due to partial exchange with nonmarine diagenetic fluids rather than an age recording later diagenetic and/or postdepositional tectonic events. Full resetting of the Rb-Sr geochronometer in glauconite that would allow dating of postdepositional or late diagenetic events requires that all analyzed grains fully equilibrate with the diagenetic fluid. We expect that this would be expressed as a nonmarine $^{87}Sr/^{86}Sr_{initial}$ in such altered glauconites and ~uniform $^{87}Sr/^{86}Sr$ composition for a given Rb/Sr ratio. Analyzed glauconites from both Arrowie and Amadeus basins, however, show considerable spreads in $\Delta^{87}Sr$ for spots with similar Rb/Sr ratios (e.g., Ajax 356; Figure 9), arguing for partial exchange with a relatively unradiogenic fluid. We therefore consider it unlikely that our "young ages" are geologically meaningful. However, full resetting or equilibration of the Rb-Sr isotope system in glauconite grains and their alteration products is likely to occur in other settings with more intense fluid-rock interaction. The interpretative framework established here will assist in the evaluation of circumstances where this is potentially the case, facilitating dating of specific postdepositional or tectonic events. Further and more systematic work is needed to test these scenarios.

4.3.2. Origin and Significance of Excessively Old Glauconite Rb-Sr Ages

Interestingly, some altered grains in classes containing carbonate inclusions return ages that are older than noninclusion-bearing $GL_{illitised}$ and $GL_{pristine}$ grains (Ajax samples) and, in the case of H41_320, also older than the expected stratigraphic age (Figure 8). Indeed, carbonate-inclusion-bearing grains are commonly associated

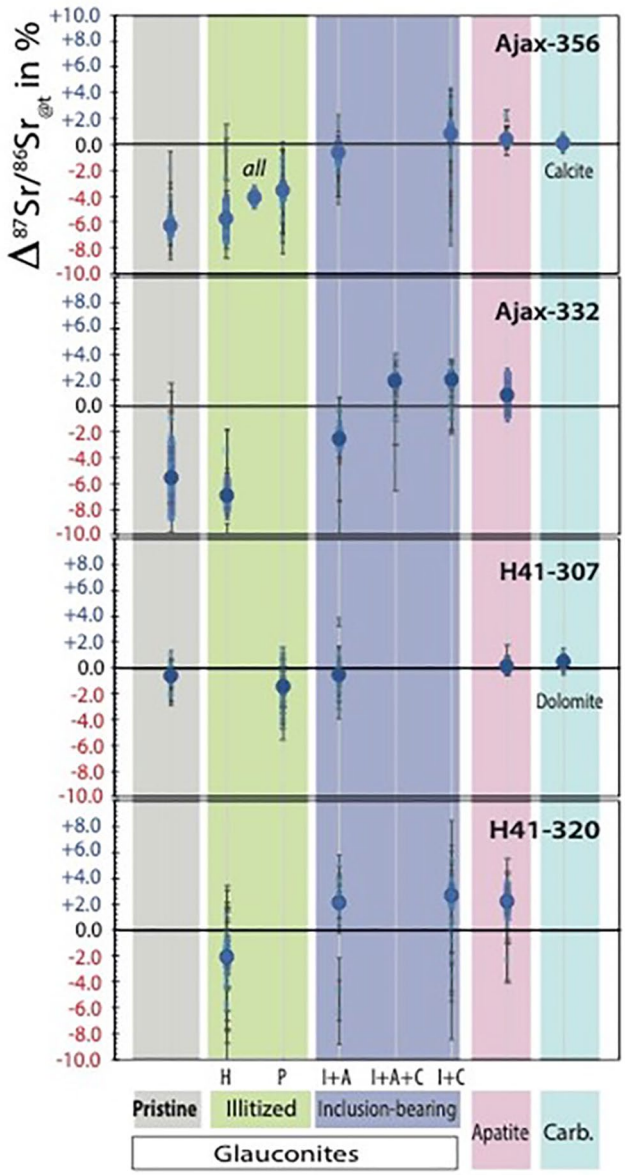

Figure 10. Weighted mean $\Delta^{87}Sr_t$ for each sample and alteration class, with full uncertainty propagation. $\Delta^{87}Sr_t$ of individual analyses and their propagated uncertainties are also shown.

with somewhat more radiogenic $^{87}Sr/^{86}Sr$ values than predicted based on their measured Rb/Sr, stratigraphic age and assuming isotopic equilibration with coeval seawater (Figures 9 and 10; Figure S3 in Supporting Information S1). Such excessively "old" ages with more radiogenic Sr signatures are most commonly attributed to incomplete maturation leading to the (partial) retention of the inherited and thus older detrital substrate phases (Derkowski et al., 2009; Hower et al., 1963; Hurley et al., 1959). However, we find (a) no petrographic evidence for detrital inclusions in these "older" spots; (b) excessively radiogenic glauconite cooccurs with "younger" and ^{87}Sr depleted glauconite; and (c) the shape, size and fabric of these "older" glauconite pellets to be entirely consistent with authigenic clay rather than purported detrital phases; a different mechanism(s) must therefore be responsible for the observed more radiogenic Sr data and associated "old" ages.

Unlike glauconite, carbonates can incorporate relatively great amounts of Sr, which is of diagenetic origin, non-marine and highly radiogenic Sr. Petrographic and geochemical observations demonstrate a burial diagenetic origin for the carbon inclusions (see Section 4.2) so that the ages obtained for carbonate-bearing samples must be considered to represent isotopic mixing ages. We propose that the precipitation of secondary carbonate inclusions from diagenetic fluids shifted the Rb-Sr to lower values, potentially resulting in "older" ages. The observation of a mixing array toward a highly radiogenic Sr endmember (see Figures 6 and 7; Figure S3 in Supporting Information S1) suggests that at least some of these carbonate inclusions also captured highly radiogenic Sr sourced from the dissolution of ambient Rb-rich and highly radiogenic mineral phases such as detrital mica and/or K-feldspar, resulting in anomalously high $^{87}Sr/^{86}Sr$ values in affected glauconites. Consistent with this, data points classified as GL_{I+C} and GL_{I+A+C} show $\Delta^{87}Sr$ values that are almost uniformly $\geq 0\%$ (Figures 9 and 10). Perhaps future studies can compare the results of in situ laser ablation Rb-Sr technique with the conventional technique where samples can be treated by acid to eliminate the effect of carbonates.

4.3.3. True Depositional Age From Apatite-Bearing, Petrographically Unaltered Glauconite?

Petrographic considerations and their common cooccurrence in recent sediments suggest that apatite is cogenetic with glauconite in our sample set (see Section 4.3). This is also supported by the distribution of $\Delta^{87}Sr$ for apatite-bearing samples that is centered around 0% and is therefore quite distinct from that of calcite inclusion-bearing grains (Figure S6 in Supporting Information S1). Apatite-bearing but otherwise pristine glauconite grains in sample H41_307 return an age that overlaps with the expected stratigraphic age of the Tempe Fm (Figure 9) as well as an $^{87}Sr/^{86}Sr_{initial}$ that is very similar to the early Cambrian seawater value of ~0.709 (Table 2). Overall, apatite-bearing glauconite, except for H41-320, yield ages closer to the stratigraphic ages (Figure 9). We suggest that the high concentration of Sr in relatively alteration-resistant apatite inclusions limits isotopic exchange of Sr in apatite-containing glauconite grains, preserving $^{87}Sr/^{86}Sr$ through diagenesis. Although our results suggest that apatite-bearing glauconite is a prospective target for obtaining Rb-Sr depositional ages in partially altered sedimentary sequences, these results are based on a limited number of samples. Perhaps further work on phosphatic glauconite in hardgrounds, which are typically well-preserved, could be very helpful to test to what extent apatite-bearing glauconite preserves a primary age in altered sequences.

5. Conclusions

The combined petrographic and in situ geochemical screening approach applied in this study allows for the differentiation of variable degrees and styles of glauconite alteration in diagenetically impacted Cambrian sedimentary

rocks. Our study shows that prealteration grain fabric and the magnitude of alteration are the controlling factors in the cooccurrence of variably preserved glauconite. Illitisation is identified as the primary alteration phase, but geochemical fingerprinting shows that diagenetic carbonate (calcite, dolomite) inclusions are a common feature even in petrographically seemingly "pristine" glauconite grains. It is shown that petrographically distinct "pristine" and illitised grains have overlapping compositions, potentially reflecting cryptic alteration and diagenetic Sr exchange with relatively unradiogenic burial. Both illitised and pristine glauconite therefore return Rb-Sr ages that are younger than the expected stratigraphic age. The presence of carbonate inclusions, in contrast, is associated with relatively older Rb-Sr ages and, in Tempe Fm sample H41_320, with an Rb-Sr age that is older than the stratigraphic age. We attribute this to diagenetic Sr incorporation in carbonates, decreasing the Rb/Sr ratio of the inclusion-bearing grains and increasing their $^{87}Sr/^{86}Sr$ ratios, where Sr is sourced from the dissolution of detrital components in the ambient sediment matrix. Both "young" and "old" ages are considered isotopic mixing ages. Glauconite containing cogenetic apatite, by contrast, returns an age consistent with the expected stratigraphic age for the Tempe Fm (~505.1 ± 5.5 Ma in sample H41_307). We attribute this to the high Sr content and low reactivity of apatite relative to glauconite, although further work on a larger number of samples is required to examine this conclusion.

Our study shows that both petrographic and geochemical screening should be considered for in situ Rb-Sr dating of glauconite. Internal texture/fabric and relative porosity/permeability of glauconite grains are also important factors to consider, especially in light of our sampling laser spot size of 85 microns of glauconite with micron-sized inclusions. While, further systematic work on an extensive number of samples is required to assess the impact of host lithology, grain fabric and permeability, as well as the impacted alteration fluid and burial on the fidelity of glauconite Rb-Sr geochronology, the ubiquity of glauconites, new technology and approaches allowing rapid petrographic, trace elemental and isotopic screening of each grain opens new possibilities to address these issues and gain new insights on the depositional and burial history of sedimentary rocks.

Data Availability Statement

The data used in this research are available in Supporting Information S1 and are also available in Figshare at https://doi.org/10.25949/21644864.

Acknowledgments
The work was supported by an Australian Government Research Training Program Scholarship to MR, a Macquarie University Research Seeding Grant CRO 19/797 (SCL, GB, and JF) as well as ARC Discovery Project DP210100462 (JF, GB, SL, and AB).

References

Abbott, A. N., Löhr, S., & Trethewy, M. (2019). Are clay minerals the primary control on the oceanic rare earth element budget? *Frontiers in Marine Science*, *6*, 504. https://doi.org/10.3389/fmars.2019.00504

Amireh, B., Jarrar, G., Henjes-Kunst, F., & Schneider, W. (1998). K-Ar dating, X-Ray diffractometry, optical and scanning electron microscopy of glauconies from the early Cretaceous Kurnub Group of Jordan. *Geological Journal*, *33*(1), 49–65. https://doi.org/10.1002/(sici)1099-1034(199801/03)33:1<49::aid-gj759>3.0.co;2-y

Baldermann, A., Dietzel, M., Mavromatis, V., Mittermayr, F., Warr, L. N., & Wemmer, K. (2017). The role of Fe on the formation and diagenesis of interstratified glauconite-smectite and illite-smectite: A case study of Upper Cretaceous shallow-water carbonates. *Chemical Geology*, *453*, 21–34. https://doi.org/10.1016/j.chemgeo.2017.02.008

Baldermann, A., Warr, L. N., Grathoff, G. H., & Dietzel, M. (2013). The rate and mechanism of deep-sea glauconite formation at the Ivory Coast–Ghana Marginal Ridge. *Clays and Clay Minerals*, *61*(3), 258–276. https://doi.org/10.1346/ccmn.2013.0610307

Baldermann, A., Warr, L., Letofsky-Papst, I., & Mavromatis, V. (2015). Substantial iron sequestration during green-clay authigenesis in modern deep-sea sediments. *Nature Geoscience*, *8*(11), 885–889. https://doi.org/10.1038/ngeo2542

Banerjee, S., Bansal, U., & Thorat, A. V. (2016). A review on palaeogeographic implications and temporal variation in glaucony composition. *Journal of Palaeogeography*, *5*(1), 43–71. https://doi.org/10.1016/j.jop.2015.12.001

Banerjee, S., Chattoraj, S. L., Saraswati, P., Dasgupta, S., & Sarkar, U. (2012). Substrate control on formation and maturation of glauconites in the Middle Eocene Harudi Formation, western Kutch, India. *Marine and Petroleum Geology*, *30*(1), 144–160. https://doi.org/10.1016/j.marpetgeo.2011.10.008

Bansal, U., Banerjee, S., Pande, K., & Ruidas, D. K. (2020). Unusual seawater composition of the Late Cretaceous Tethys imprinted in glauconite of Narmada basin, central India. *Geological Magazine*, *157*(2), 233–247. https://doi.org/10.1017/s0016756819000621

Bansal, U., Pande, K., Banerjee, S., Nagendra, R., & Jagadeesan, K. C. (2019). The timing of oceanic anoxic events in the Cretaceous succession of Cauvery Basin: Constraints from $^{40}Ar/^{39}Ar$ ages of glauconite in the Karai Shale Formation. *Geological Journal*, *54*(1), 308–315. https://doi.org/10.1002/gj.3177

Betts, M. J., Paterson, J. R., Jacquet, S. M., Andrew, A. S., Hall, P. A., Jago, J. B., et al. (2018). Early Cambrian chronostratigraphy and geochronology of South Australia. *Earth-Science Reviews*, *185*, 498–543. https://doi.org/10.1016/j.earscirev.2018.06.005

Boulesteix, T., Solé, J., Pi, T., & Cathelineau, M. (2020). Reappraisal of the GL-O reference material for K-Ar dating: New insight from microanalysis, single-grain and milligram Ar Measurements. *Geostandards and Geoanalytical Research*, *44*(2), 287–306. https://doi.org/10.1111/ggr.12306

Bradshaw, J. (1991). The Tempe Formation: An early middle Cambrian, open marine, clastic, and carbonate sequence, central Amadeus Basin. *Bureau of Mineral Resources Geology and Geophysics Bulletin*, *236*, 245–252.

Buick, I. S., Miller, J. A., Williams, I. S., & Cartwright, I. (2001). Ordovician high-grade metamorphism of a newly recognised late Neoproterozoic terrane in the northern Harts Range, central Australia. *Journal of Metamorphic Geology*, *19*(4), 373–394. https://doi.org/10.1046/j.0263-4929.2001.00316.x

Carr, L., Korsch, R. J., Struckmeyer, H. I., Jones, L. E. A., Holzscuh, J., Costelloe, R., & Meixner, A. (2012). *The architecture and petroleum potential of Australia's onshore sedimentary basins from deep seismic reflection data and petroleum systems maturation modelling: The Arrowie, Georgina and Darling Basins* (p. 84). Geoscience Australia. Record 2012/36.

Cecil, M. R., & Ducea, M. N. (2011). K–Ca ages of authigenic sediments: Examples from Paleozoic glauconite and applications to low-temperature thermochronometry. *International Journal of Earth Sciences*, *100*(8), 1783–1790. https://doi.org/10.1007/s00531-010-0618-y

Charpentier, D., Buatier, M. D., Jacquot, E., Gaudin, A., & Wheat, C. (2011). Conditions and mechanism for the formation of iron-rich Montmorillonite in deep sea sediments (Costa Rica margin): Coupling high resolution mineralogical characterization and geochemical modeling. *Geochimica et Cosmochimica Acta*, *75*(6), 1397–1410. https://doi.org/10.1016/j.gca.2010.11.026

Chaudhuri, S., & Clauer, N. (1993). Strontium isotopic compositions and potassium and rubidium contents of formation waters in sedimentary basins: Clues to the origin of the solutes. *Geochimica et Cosmochimica Acta*, *57*(2), 429–437. https://doi.org/10.1016/0016-7037(93)90441-x

Clauer, N. (1981). Rb—Sr and K—Ar dating of Precambrian clays and glauconies. *Precambrian Research*, *15*(3–4), 331–352. https://doi.org/10.1016/0301-9268(81)90056-5

Clauer, N. (2013). The K-Ar and $^{40}Ar/^{39}Ar$ methods revisited for dating fine-grained K-bearing clay minerals. *Chemical Geology*, *354*, 163–185. https://doi.org/10.1016/j.chemgeo.2013.05.030

Clauer, N., Hoffert, M., & Karpoff, A.-M. (1982). The Rb/Sr isotope system as an index of origin and diagenetic evolution of southern Pacific red clays. *Geochimica et Cosmochimica Acta*, *46*(12), 2659–2664. https://doi.org/10.1016/0016-7037(82)90384-2

Clauer, N., Keppens, E., & Stille, P. (1992). Sr isotopic constraints on the process of glauconitization. *Geology*, *20*(2), 133–136. https://doi.org/10.1130/0091-7613(1992)020<0133:sicotp>2.3.co;2

Cox, G. M., Isakson, V., Hoffman, P. F., Gernon, T. M., Schmitz, M. D., Shahin, S., et al. (2018). South Australian U-Pb zircon (CA-ID-TIMS) age supports globally synchronous Sturtian deglaciation. *Precambrian Research*, *315*, 257–263. https://doi.org/10.1016/j.precamres.2018.07.007

Denison, R., Koepnick, R., Burke, W., & Hetherington, E. (1998). Construction of the Cambrian and Ordovician seawater $^{87}Sr/^{86}Sr$ curve. *Chemical Geology*, *152*(3–4), 325–340. https://doi.org/10.1016/s0009-2541(98)00119-3

Derkowski, A., Środoń, J., Franus, W., Uhlík, P., Banaś, M., Zielinski, G., et al. (2009). Partial dissolution of glauconitic samples: Implications for the methodology of K-Ar and Rb-Sr dating. *Clays and Clay Minerals*, *57*(5), 531–554. https://doi.org/10.1346/ccmn.2009.0570503

Dickin, A. P. (2018). *Radiogenic isotope geology*. Cambridge University Press.

Du, X., Lu, Y., Duan, D., Liu, Z., Zhao, K., Jia, J., & Fu, H. (2020). Was volcanic activity during the Ordovician-Silurian transition in South China part of a global phenomenon? Constraints from zircon U–Pb dating of volcanic ash beds in black shales. *Marine and Petroleum Geology*, *114*, 104209. https://doi.org/10.1016/j.marpetgeo.2019.104209

Du Vivier, A. D., Selby, D., Sageman, B. B., Jarvis, I., Gröcke, D. R., & Voigt, S. (2014). Marine $^{187}Os/^{188}Os$ isotope stratigraphy reveals the interaction of volcanism and ocean circulation during Oceanic Anoxic Event 2. *Earth and Planetary Science Letters*, *389*, 23–33. https://doi.org/10.1016/j.epsl.2013.12.024

Farkas, J., Collins, A., Al Sarakhi, H., Chakrabarti, R., Reeda, A., Löhr, S. C., et al. (2018). Towards improved stratigraphy of Proterozoic Basins: Telling the time from a single glauconite grain based on in-situ Rb/Sr dating. In *AGCC Abstract, Australian Geoscience Council Convetions, Adelaide* (p. 238).

Foden, J., Elburg, M. A., Dougherty-Page, J., & Burtt, A. (2006). The timing and duration of the Delamerian Orogeny: Correlation with the Ross Orogen and implications for Gondwana assembly. *The Journal of Geology*, *114*(2), 189–210. https://doi.org/10.1086/499570

Foland, K. A., Linder, J. S., Laskowski, T. E., & Grant, N. K. (1984). $^{40}Ar^{39}Ar$ dating of glauconites: Measured ^{39}Ar recoil loss from well-crystallized specimens. *Chemical Geology*, *46*(3), 241–264. https://doi.org/10.1016/0009-2541(84)90192-x

Frank, A. B., Klaebe, R. M., Löhr, S. C., Xu, L., & Frei, R. (2020). Chromium isotope composition of organic-rich marine sediments and their mineral phases and implications for using black shales as a paleoredox archive. *Geochimica et Cosmochimica Acta*, *270*, 338–359. https://doi.org/10.1016/j.gca.2019.11.035

Gaudin, A., Buatier, M. D., Beaufort, D., Petit, S., Grauby, O., & Decarreau, A. (2005). Characterization and origin of Fe^{3+}-Montmorillonite in deep-water calcareous sediments (Pacific Ocean, Costa Rica margin). *Clays and Clay Minerals*, *53*(5), 452–465. https://doi.org/10.1346/ccmn.2005.0530503

Gopalan, K. (2008). Conjunctive K–Ca and Rb–Sr dating of glauconies. *Chemical Geology*, *247*(1–2), 119–123. https://doi.org/10.1016/j.chemgeo.2007.10.004

Gorojovsky, L., & Alard, O. (2020). Optimisation of laser and mass spectrometer parameters for the in situ analysis of Rb/Sr ratios by LA-ICP-MS/MS. *Journal of Analytical Atomic Spectrometry*, *35*(10), 2322–2336. https://doi.org/10.1039/d0ja00308e

Grant, N. K., Laskowski, T. E., & Foland, K. (1984). Rb/Sr and K/Ar ages of Paleozoic glauconites from Ohio—Indiana and Missouri, USA. *Chemical Geology*, *46*(3), 217–239. https://doi.org/10.1016/0009-2541(84)90191-8

Gravestock, D. I. (1984). Archaeocyatha from lower parts of the Lower Cambrian carbonate sequence in South Australia.

Griffin, W., Powell, W., Pearson, N. J., & O'Reilly, S. G. (2008). GLITTER: Data reduction software for laser ablation ICP-MS. *Short Course Series*, *40*, 308–311.

Griffis, N. P., Montañez, I. P., Mundil, R., Richey, J., Isbell, J., Fedorchuk, N., et al. (2019). Coupled stratigraphic and U-Pb zircon age constraints on the late Paleozoic icehouse-to-greenhouse turnover in south-central Gondwana. *Geology*, *47*(12), 1146–1150. https://doi.org/10.1130/g46740.1

Griffis, N. P., Mundil, R., Montañez, I. P., Isbell, J., Fedorchuk, N., Vesely, F., et al. (2018). A new stratigraphic framework built on U-Pb single-zircon TIMS ages and implications for the timing of the penultimate icehouse (Paraná Basin, Brazil). *GSA Bulletin*, *130*(5–6), 848–858. https://doi.org/10.1130/b31775.1

Guimaraes, E. M., Velde, B., Hillier, S., & Nicot, E. (2000). Diagenetic/anchimetamorphic changes on the Proterozoic glauconite and glaucony from the Paranoa group, mid-western Brazil. *Revista Brasileira de Geociencias*, *30*(3), 363–366. https://doi.org/10.25249/0375-7536.2000303363366

Han, S., Löhr, S., Abbott, A. N., Baldermann, A., Farkas, J., McMahon, W., et al. (2022). Earth system science applications of next-generation SEM-EDS automated mineral mapping. *Frontiers in Earth Science*, *10*, 2244. https://doi.org/10.3389/feart.2022.956912

Hand, M., Mawby, J., Kinny, P., & Foden, J. (1999). U–Pb ages from the Harts Range, central Australia: Evidence for early Ordovician extension and constraints on Carboniferous metamorphism. *Journal of the Geological Society*, *156*(4), 715–730. https://doi.org/10.1144/gsjgs.156.4.0715

Hogmalm, K. J., Zack, T., Karlsson, A. K.-O., Sjöqvist, A. S., & Garbe-Schönberg, D. (2017). In situ Rb–Sr and K–Ca dating by LA-ICP-MS/MS: An evaluation of N_2O and SF_6 as reaction gases. *Journal of Analytical Atomic Spectrometry*, *32*(2), 305–313. https://doi.org/10.1039/c6ja00362a

Hower, J. (1961). Some factors concerning the nature and origin of glauconite. *American Mineralogist*, *46*, 313–334.

Hower, J., Hurley, P., Pinson, W., & Fairbairn, H. (1963). The dependence of K-Ar age on the mineralogy of various particle size ranges in a shale. *Geochimica et Cosmochimica Acta*, *27*(5), 405–410. https://doi.org/10.1016/0016-7037(63)90080-2

Huff, W. D., Bergström, S. M., & Kolata, D. R. (1992). Gigantic Ordovician volcanic ash fall in North America and Europe: Biological, tectonomagmatic, and event-stratigraphic significance. *Geology*, *20*(10), 875–878. https://doi.org/10.1130/0091-7613(1992)020<0875:govafi>2.3.co;2

Hurley, P. (1966). *K-Ar dating of sediments, Potassium argon dating* (pp. 134–151). Springer.

Hurley, P., Fisher, N., Pinson, W., Jr., & Fairbairn, H. (1961). Geochronology of Proterozoic granites in Northern Territory, Australia. Part 1: K-Ar and Rb-Sr age determinations. *Geological Society of America Bulletin*, *72*(5), 653–662. https://doi.org/10.1130/0016-7606(1961)72[653:gopgin]2.0.co;2

Hurley, P. M., Boucot, A., Albee, A., Faul, H., Pinson, W., & Fairbairn, H. W. (1959). Minimum age of the Lower Devonian slate near Jackman, Maine. *Geological Society of America Bulletin*, *70*(7), 947–950. https://doi.org/10.1130/0016-7606(1959)70[947:maotld]2.0.co;2

Hurley, P. M., Cormier, R. F., Hower, J., Fairbairn, H., & Pinson, W., Jr. (1960). Reliability of glauconite for age measurement by K-Ar and Rb-Sr methods. *AAPG Bulletin*, *44*, 1793–1808.

Jago, J. B., Zang, W.-L., Sun, X., Brock, G. A., Paterson, J. R., & Skovsted, C. B. (2006). A review of the Cambrian biostratigraphy of South Australia. *Palaeoworld*, *15*(3–4), 406–423. https://doi.org/10.1016/j.palwor.2006.10.014

James, N. P., & Gravestock, D. I. (1990). Lower Cambrian shelf and shelf margin buildups, Flinders ranges, South Australia 1. *Sedimentology*, *37*(3), 455–480. https://doi.org/10.1111/j.1365-3091.1990.tb00147.x

Jarrett, A., Edwards, D., Boreham, C., & McKirdy, D. (2016). Petroleum geochemistry of the Amadeus Basin. In *AGES 2016 Proceedings* (pp. 37–42). NT Geological Survey.

Jochum, K., Weis, U., Stoll, B., Kuzmin, D., Yang, Q., Raczek, I., et al. (2011). Determination of reference values for NIST SRM 610-617 glasses following ISO guidelines. *Geostandards and Geoanalytical Research*, *35*(4), 397–429. https://doi.org/10.1111/j.1751-908x.2011.00120.x

Jourdan, F., Féraud, G., Bertrand, H., Kampunzu, A. B., Tshoso, G., Watkeys, M. K., & Le Gall, B. (2005). Karoo large igneous province: Brevity, origin, and relation to mass extinction questioned by new $^{40}Ar/^{39}Ar$ age data. *Geology*, *33*(9), 745–748. https://doi.org/10.1130/g21632.1

Jourdan, F., Marzoli, A., Bertrand, H., Cirilli, S., Tanner, L. H., Kontak, D. J., et al. (2009). $^{40}Ar/^{39}Ar$ ages of CAMP in North America: Implications for the Triassic–Jurassic boundary and the 40 K decay constant bias. *Lithos*, *110*(1–4), 167–180. https://doi.org/10.1016/j.lithos.2008.12.011

Kelly, J. C., Webb, J. A., & Maas, R. (2001). Isotopic constraints on the genesis and age of autochthonous glaucony in the Oligo-Miocene Torquay Group, south-eastern Australia. *Sedimentology*, *48*(2), 325–338. https://doi.org/10.1046/j.1365-3091.2001.00365.x

Kendall, B., Creaser, R. A., & Selby, D. J. G. (2006). Re-Os geochronology of postglacial black shales in Australia: Constraints on the timing of "Sturtian" glaciation. *Geology*, *34*(9), 729–732. https://doi.org/10.1130/g22775.1

Kendall, B. S., Creaser, R. A., Ross, G. M., & Selby, D. (2004). Constraints on the timing of Marinoan "Snowball Earth" glaciation by $^{187}Re–^{187}Os$ dating of a Neoproterozoic, post-glacial black shale in Western Canada. *Earth and Planetary Science Letters*, *222*(3–4), 729–740. https://doi.org/10.1016/j.epsl.2004.04.004

Keppens, E., & Pasteels, P. (1982). Comment on the paper: "A test of the reliability of the Rb-Sr dates for selected glauconite morphologies of the Upper Cretaceous (Navesink Formation) of New Jersey", by RL Montag and DE Seidemann. *Earth and Planetary Science Letters*, *58*(3), 439–441. https://doi.org/10.1016/0012-821x(82)90092-9

Lanson, B., Beaufort, D., Berger, G., Bauer, A., Cassagnabere, A., & Meunier, A. (2002). Authigenic kaolin and illitic minerals during burial diagenesis of sandstones: A review. *Clay Minerals*, *37*, 1–22. https://doi.org/10.1180/0009855023710014

López-Quirós, A., Escutia, C., Sánchez-Navas, A., Nieto, F., Garcia-Casco, A., Martín-Algarra, A., et al. (2019). Glaucony authigenesis, maturity and alteration in the Weddell Sea: An indicator of paleoenvironmental conditions before the onset of Antarctic glaciation. *Scientific Reports*, *9*, 1–12. https://doi.org/10.1038/s41598-019-50107-1

López-Quirós, A., Sánchez-Navas, A., Nieto, F., & Escutia, C. (2020). New insights into the nature of glauconite. *American Mineralogist: Journal of Earth and Planetary Materials*, *105*(5), 674–686. https://doi.org/10.2138/am-2020-7341

Lúcio, T., Neto, J. A. S., & Selby, D. (2020). Late Barremian/early Aptian Re–Os age of the Ipubi Formation black shales: Stratigraphic and paleoenvironmental implications for Araripe Basin, northeastern Brazil. *Journal of South American Earth Sciences*, *102*, 102699. https://doi.org/10.1016/j.jsames.2020.102699

Maidment, D. W., Hand, M., & Williams, I. S. (2006). A time frame for protracted multiphase metamorphism, magmatism and deformation in the exhumed core of the Alice Springs Orogen, Harts Range, central Australia. In *ASEG Extended Abstracts 2006* (pp. 1–4).

Morton, J. P., & Long, L. E. (1980). Rb-Sr dating of Paleozoic glauconite from the Llano region, central Texas. *Geochimica et Cosmochimica Acta*, *44*(5), 663–672. https://doi.org/10.1016/0016-7037(80)90156-8

Obradovich, J. D. (1988). A different perspective on glauconite as a chronometer for geologic time scale studies. *Paleoceanography*, *3*(6), 757–770. https://doi.org/10.1029/pa003i006p00757

O'Brien, G., Milnes, A., Veeh, H., Heggie, D., Riggs, S., Cullen, D., et al. (1990). Sedimentation dynamics and redox iron-cycling: Controlling factors for the apatite—glauconite association on the East Australian continental margin. *Geological Society, London, Special Publications*, *52*(1), 61–86. https://doi.org/10.1144/gsl.sp.1990.052.01.06

Odin, G. (1982). Interlaboratory standards for dating purposes. In *Numerical dating in stratigraphy* (Vol. 1, pp. 123–148). John Wiley & Sons.

Odin, G. S., & Matter, A. (1981). De glauconiarum origine. *Sedimentology*, *28*(5), 611–641. https://doi.org/10.1111/j.1365-3091.1981.tb01925.x

Peng, S., Babcock, L., & Ahlberg, P. (2020). *The Cambrian Period, Geologic Time Scale 2020* (pp. 565–629). Elsevier.

Pevear, D. R. (1999). Illite and hydrocarbon exploration. *Proceedings of the National Academy of Sciences*, *96*(7), 3440–3446. https://doi.org/10.1073/pnas.96.7.3440

Prave, A. R., Condon, D. J., Hoffmann, K. H., Tapster, S., & Fallick, A. E. (2016). Duration and nature of the end-Cryogenian (Marinoan) glaciation. *Geology*, *44*(8), 631–634. https://doi.org/10.1130/g38089.1

Rafiei, M., & Kennedy, M. J. (2019). Weathering in a world without terrestrial life recorded in the Mesoproterozoic Velkerri Formation. *Nature Communications*, *10*(1), 3448. https://doi.org/10.1038/s41467-019-11421-4

Rafiei, M., Löhr, S. C., Baldermann, A., Webster, R., & Kong, C. (2020). Quantitative petrographic differentiation of detrital vs diagenetic clay minerals in marine sedimentary sequences: Implications for the rise of biotic soils. *Precambrian Research*, *350*, 105948. https://doi.org/10.1016/j.precamres.2020.105948

Redaa, A., Farkaš, J., Gilbert, S., Collins, A. S., Löhr, S., Vasegh, D., et al. (2022). Testing nano-powder and fused-glass mineral reference materials for in situ Rb-Sr dating of glauconite, phlogopite, biotite and feldspar via LA-ICP-MS/MS. *Geostandards and Geoanalytical Research*, *47*(1), 23–48. https://doi.org/10.1111/ggr.12467

Redaa, A., Farkaš, J., Gilbert, S., Collins, A. S., Wade, B., Löhr, S. C., et al. (2021). Assessment of elemental fractionation and matrix effects during in situ Rb–Sr dating of phlogopite by LA-ICP-MS/MS: Implications for the accuracy and precision of mineral ages. *Journal of Analytical Atomic Spectrometry*, *36*(2), 322–344. https://doi.org/10.1039/d0ja00299b

Rooney, A. D., Macdonald, F. A., Strauss, J. V., Dudás, F. Ö., Hallmann, C., & Selby, D. (2014). Re-Os geochronology and coupled Os-Sr isotope constraints on the Sturtian snowball Earth. *Proceedings of the National Academy of Sciences*, *111*(1), 51–56. https://doi.org/10.1073/pnas.1317266110

Rousset, D., Leclerc, S., Clauer, N., Lancelot, J. L., Cathelineau, M., & Aranyossy, J.-F. O. (2004). Age and origin of Albian glauconites and associated clay minerals inferred from a detailed geochemical analysis. *Journal of Sedimentary Research*, *74*(5), 631–642. https://doi.org/10.1306/031104740631

Schaltegger, U., Schmitt, A., & Horstwood, M. (2015). U–Th–Pb zircon geochronology by ID-TIMS, SIMS, and laser ablation ICP-MS: Recipes, interpretations, and opportunities. *Chemical Geology*, *402*, 89–110. https://doi.org/10.1016/j.chemgeo.2015.02.028

Scheiblhofer, E., Moser, U., Löhr, S., Wilmsen, M., Farkaš, J., Gallhofer, D., et al. (2022). Revisiting glauconite geochronology: Lessons learned from in situ radiometric dating of a glauconite-rich Cretaceous Shelfal sequence. *Minerals*, *12*(7), 818. https://doi.org/10.3390/min12070818

Schmid, S. (2017). Chemostratigraphy and palaeo-environmental characterisation of the Cambrian stratigraphy in the Amadeus Basin, Australia. *Chemical Geology*, *451*, 169–182. https://doi.org/10.1016/j.chemgeo.2017.01.019

Selby, D. (2009). U-Pb zircon geochronology of the Aptian/Albian boundary implies that the GL-O international glauconite standard is anomalously young. *Cretaceous Research*, *30*(5), 1263–1267. https://doi.org/10.1016/j.cretres.2009.07.001

Shaw, R., Stewart, A. T., & Black, L. (1984). The Arunta Inlier: A complex ensialic mobile belt in central Australia. Part 2: Tectonic history. *Australian Journal of Earth Sciences*, *31*(4), 457–484. https://doi.org/10.1080/08120098408729305

Shaw, R. D., Etheridge, M. A., & Lambeck, K. (1991). Development of the Late Proterozoic to Mid-Paleozoic, intracratonic Amadeus Basin in central Australia: A key to understanding tectonic forces in plate interiors. *Tectonics*, *10*(4), 688–721. https://doi.org/10.1029/90tc02417

Smalley, P., Forsberg, A., & Råheim, A. (1987). RbSr dating of fluid migration in hydrocarbon source rocks. *Chemical Geology*, *65*(3–4), 223–233. https://doi.org/10.1016/0168-9622(87)90005-4

Smith, P. E., Evensen, N. M., York, D., & Odin, G. S. (1998). Single-grain ^{40}Ar-^{39}Ar ages of glauconies: Implications for the geologic time scale and global sea level variations. *Science*, *279*(5356), 1517–1519. https://doi.org/10.1126/science.279.5356.1517

Smith, P. M., Brock, G. A., & Paterson, J. R. (2015). Fauna and biostratigraphy of the Cambrian (Series 2, Stage 4; Ordian) Tempe Formation (Pertaoorrta Group), Amadeus Basin, Northern Territory. *Alcheringa: An Australasian Journal of Palaeontology*, *39*(1), 40–70. https://doi.org/10.1080/03115518.2014.951917

Stille, P., & Clauer, N. (1994). The process of glauconitization: Chemical and isotopic evidence. *Contributions to Mineralogy and Petrology*, *117*(3), 253–262. https://doi.org/10.1007/bf00310867

Straeten, C. A. V. (2004). K-bentonites, volcanic ash preservation, and implications for Early to Middle Devonian volcanism in the Acadian orogen, eastern North America. *Geological Society of America Bulletin*, *116*(3), 474–489. https://doi.org/10.1130/b25244.1

Tillberg, M., Drake, H., Zack, T., Hogmalm, J., & Åström, M. (2017). In situ Rb-Sr dating of fine-grained vein mineralizations using LA-ICP-MS. *Procedia Earth and Planetary Science*, *17*, 464–467. https://doi.org/10.1016/j.proeps.2016.12.117

Tillberg, M., Drake, H., Zack, T., Kooijman, E., Whitehouse, M. J., & Åström, M. E. (2020). In situ Rb-Sr dating of slickenfibres in deep crystalline basement faults. *Scientific Reports*, *10*, 1–13. https://doi.org/10.1038/s41598-019-57262-5

Tóth, E., Weiszburg, T. G., Jeffries, T., Williams, C. T., Bartha, A., Bertalan, É., & Cora, I. (2010). Submicroscopic accessory minerals overprinting clay mineral REE patterns (celadonite–glauconite group examples). *Chemical Geology*, *269*(3–4), 312–328. https://doi.org/10.1016/j.chemgeo.2009.10.006

Veizer, J., Ala, D., Azmy, K., Bruckschen, P., Buhl, D., Bruhn, F., et al. (1999). ^{87}Sr/^{86}Sr, δ^{13}C and δ^{18}O evolution of Phanerozoic seawater. *Chemical Geology*, *161*(1–3), 59–88. https://doi.org/10.1016/s0009-2541(99)00081-9

Vermeesch, P. (2018). IsoplotR: A free and open toolbox for geochronology. *Geoscience Frontiers*, *9*(5), 1479–1493. https://doi.org/10.1016/j.gsf.2018.04.001

Villa, I. M., De Bièvre, P., Holden, N., & Renne, P. (2015). IUPAC-IUGS recommendation on the half life of 87Rb. *Geochimica et Cosmochimica Acta*, *164*, 382–385. https://doi.org/10.1016/j.gca.2015.05.025

Wang, D., Zhu, X.-K., Zhao, N., Yan, B., Li, X.-H., Shi, F., & Zhang, F. (2019). Timing of the termination of Sturtian glaciation: SIMS U-Pb zircon dating from South China. *Journal of Asian Earth Sciences*, *177*, 287–294. https://doi.org/10.1016/j.jseaes.2019.03.015

Wiman, C. (1903). *Studien über das nordbaltische Silurgebiet*. Almqvist & Wiksell.

Wotzlaw, J.-F., Hüsing, S. K., Hilgen, F. J., & Schaltegger, U. (2014). High-precision zircon U–Pb geochronology of astronomically dated volcanic ash beds from the Mediterranean Miocene. *Earth and Planetary Science Letters*, *407*, 19–34. https://doi.org/10.1016/j.epsl.2014.09.025

York, D., Evensen, N. M., Martınez, M. L., & De Basabe Delgado, J. (2004). Unified equations for the slope, intercept, and standard errors of the best straight line. *American Journal of Physics*, *72*(3), 367–375. https://doi.org/10.1119/1.1632486

Zack, T., & Hogmalm, K. J. (2016). Laser ablation Rb/Sr dating by online chemical separation of Rb and Sr in an oxygen-filled reaction cell. *Chemical Geology*, *437*, 120–133. https://doi.org/10.1016/j.chemgeo.2016.05.027

Zaitseva, T., Gorokhov, I., Ivanovskaya, T., Semikhatov, M., Kuznetsov, A., Mel'nikov, N., et al. (2008). Mössbauer characteristics, mineralogy and isotopic age (Rb-Sr, K-Ar) of Upper Riphean glauconites from the UK Formation, the Southern Urals. *Stratigraphy and Geological Correlation*, *16*(3), 227–247. https://doi.org/10.1134/s0869593808030015

Zhao, T., Algeo, T. J., Feng, Q., Zi, J.-W., & Xu, G. (2019). Tracing the provenance of volcanic ash in Permian–Triassic boundary strata, South China: Constraints from inherited and syn-depositional magmatic zircons. *Palaeogeography, Palaeoclimatology, Palaeoecology*, *516*, 190–202. https://doi.org/10.1016/j.palaeo.2018.12.002

Zhou, C., Huyskens, M. H., Lang, X., Xiao, S., & Yin, Q.-Z. (2019). Calibrating the terminations of Cryogenian global glaciations. *Geology*, *47*(3), 251–254. https://doi.org/10.1130/g45719.1